

# An Atlas of Classical Pyrochlore Spin Liquids

Daniel Lozano-Gómez,<sup>1,2</sup> Owen Benton,<sup>3</sup> Michel J. P. Gingras,<sup>2</sup> and Han Yan (闫寒)<sup>4,\*</sup>

<sup>1</sup>*Institut für Theoretische Physik and Würzburg-Dresden Cluster of Excellence ct.qmat,  
Technische Universität Dresden, 01062 Dresden, Germany*

<sup>2</sup>*Department of Physics and Astronomy, University of Waterloo, Waterloo, Ontario N2L 3G1, Canada*

<sup>3</sup>*School of Physical and Chemical Sciences, Queen Mary University of London, London, E1 4NS, United Kingdom*

<sup>4</sup>*Institute for Solid State Physics, The University of Tokyo, Kashiwa, Chiba 277-8581, Japan*

(Dated: November 7, 2024)

The pyrochlore lattice magnet has been one of the most fruitful platforms for the experimental and theoretical search for spin liquids. Besides the canonical case of spin ice, works in recent years have identified a variety of new quantum and classical spin liquids from the generic nearest-neighbor anisotropic spin Hamiltonian on the pyrochlore lattice. However, a general framework for the thorough classification and characterization of these exotic states of matter has been lacking, and so is an *exhaustive* list of all possible spin liquids that this model can support and what is the corresponding structure of their emergent field theory. In this work, we develop such a theoretical framework to allocate interaction parameters stabilizing different classical spin liquids and derive their corresponding effective generalized Gauss’s laws at low temperatures. Combining this with Monte Carlo simulations, we systematically identify all classical spin liquids for the general nearest-neighbor anisotropic spin Hamiltonian on the pyrochlore lattice. We uncover new spin liquid models with exotic forms of generalized Gauss’s law and multipole conservation laws. Furthermore, we present an atlas of all spin liquid regimes in the phase diagram, which illuminates the global picture of how different classical spin liquids are connected in parameter space and transition into each other. Our work serves as a treasure map for the theoretical study of classical and quantum spin liquids, as well as for the experimental search and rationalization of exotic pyrochlore lattice magnets.

## I. INTRODUCTION

In the past thirty years, the exploration of quantum and classical spin liquids (CSLs) stable down to the lowest temperature has been one of the most active pursuits in the study of many-body physics [1–8]. These phases, whose spins are disordered yet highly correlated, develop at low temperatures and are described by effective gauge theories emerging from the microscopic spin degrees of freedom (DOFs). Classical spin liquids often realize the electrostatics sector of gauge theories [9–11]. Upon introducing proper quantum dynamics, these CSLs may become quantum spin liquids, whose topological entanglement, fractionalized excitations, and (in the gapped case) topological order are among the most fascinating aspects of quantum matter. Classical spin liquids usually require fine-tuned spin-spin interactions on specific lattice geometry, often with geometric lattice frustration [12], to support the extensively degenerate classical ground states [2, 3] that are at the origin of their collective paramagnetic nature [13].

In particular, the pyrochlore lattice, a network of corner-sharing tetrahedra [14–16], has provided a fruitful landscape for the search of spin liquids. The first, and most canonical example is the classical spin ice [17–20], experimentally realized in  $\text{Ho}_2\text{Ti}_2\text{O}_7$  [17, 21–23] and  $\text{Dy}_2\text{Ti}_2\text{O}_7$  [24, 25]. At low temperatures, this classical spin liquid realizes an effective Maxwell U(1) elec-

trostatics theory on the parent (or premedial) diamond lattice, whose ground states are charge-free divergence-free “electric field” configurations, and elementary excitations are sources and sinks (i.e. “charges”) of that field <sup>1</sup>. In other materials [16], in which quantum effects [27] are expected to be more important than in the  $(\text{Ho,Dy})_2(\text{Ti,Sn,Ge})_2\text{O}_7$  classical spin ice compounds [28], a quantum counterpart of spins ice realizing full-fledged quantum electrodynamics, namely quantum spin ice [6, 29], has been under intense theoretical [30–40] and experimental investigations [41–49].

Zooming out to the entire landscape, a much wider spectrum of exotic classical spin liquids have been discovered upon considering the generic nearest-neighbor anisotropic bilinear spin model on the pyrochlore lattice. This family of models, parameterized by four symmetry-allowed anisotropic spin-spin couplings of exchange origin ( $\{J_{zz}, J_{\pm}, J_{\pm\pm}, J_{z\pm}\}$  [50–54]), has been successful in characterizing the low-temperature physics of various pyrochlore compounds  $\text{R}_2\text{M}_2\text{O}_7$ , where R is a trivalent rare earth ion and M is a non-magnetic tetravalent transition metal [14].

These classical spin liquids are characterized by low-energy emergent *generalized* Gauss’s laws [9, 10, 55–57]. Among them, classical spin ice [17], the Heisenberg antiferromagnet (HAFM) spin liquid [58, 59] and the XXZ model [60] host one or several copies of emergent Maxwell

\* hanyan@issp.u-tokyo.ac.jp

<sup>1</sup> Often, the dual language of magnetic field and magnetic monopoles is used in the literature [6, 26].

Gauss’s law. Other cases discovered more recently, such as the so-called pinch-line spin liquid [61] and the rank-1–rank-2 spin liquid [62] are more exotic: they are *higher-rank* spin liquids, whose generalized Gauss’s laws are imposed on tensorial (rank-2) electric fields. Such more complex versions of electrodynamics, which are allowed on the lattice due to a lack of Lorentz or rotational symmetry, describe new gapless quantum spin liquids, and are closely related to the field of fractonic states of matter [63–65]. The intrinsic multipole conservation and subsystem symmetries showcased by these higher-rank spin liquids are at the root of a rich variety of physics, from immobile fractionalized excitations dubbed fractons [56, 57, 66] to quantum error-correction [67, 68].

Apart from spin ice that occupies a three-dimensional parameter space at zero temperature, the other classical pyrochlore spin liquids that have been theoretically discovered generally live on the phase boundary of two or more magnetically ordered phases. While the phase diagram of the possible magnetic orders for the general Hamiltonian has been discussed in detail in the literature [15, 16, 53, 69] (for a recent in-depth analysis of the irrep fields, and the geometry and topology of the phases and phase boundaries, see recent work by Chung [54]), a theoretical framework to identify systematically all CSLs on the pyrochlore lattice is still lacking. This raises an important question in terms of the search for novel magnetic states of matter and whether other overlooked spin liquids exist in the phase diagram. Furthermore, an “atlas” of classical spin liquids, i.e., a map showing the exact regions in parameter space of CSLs, their dualities, and how different CSLs connect/transition into each other is still absent.

In this work, we develop such a theoretical framework based on irreducible representations and their intertetrahedra constraints, which enables a comprehensive study of various pyrochlore classical spin liquids. Specifically, we have identified *all* the classical spin liquids stabilized down to the lowest temperatures on the most generic nearest-neighbor Hamiltonian on the pyrochlore lattice. Our theory also provides a straightforward recipe for constructing the low energy effective generalized Gauss’s law for the different CSLs. We have found in total nine classical spin liquids and derived their generalized electrostatics theory, including two cases not previously discussed in previous literature and which realize Maxwell and a rank-2 U(1) electrostatics, respectively. This allows us to further chart an “atlas” of classical pyrochlore spin liquids, presenting both the exact parameter spaces of different CSLs, and a bird’s-eye view of the dualities, connectivity, and phase transition between them.

Motivated by all these considerations, we thus provide in this paper the first complete list of classical spin liquids on the pyrochlore lattice and introduce a powerful theoretical scheme for constructing their associated gauge theory. This transforms the theoretical search for pyrochlore CSLs from smart craftsmanship to a rigorously

organized systematic pursuit. Our work is also highly experimentally relevant: as shown in various previous studies [15, 48, 52, 53, 70–73], it turns out that, rather interestingly, many pyrochlore compounds find themselves rather close to the phase boundaries of semi-classical long-range magnetic orders where such multi-phase competition is critical for understanding their physics. Our work, charting out the CSLs that live on these phase boundaries, will be an important reference to understand the exotic physics at play in past and future experiments. In particular, we demonstrate the exciting opportunities to realize fracton physics in these frustrated magnetic systems. Our atlas also provides a road-map for the systematic hunt of pyrochlore quantum spin liquids, as it highlights the parameter spaces of most intense competition between the spin-spin interactions and indicates the potential nature of the prospective quantum spin liquids descending from their classical limits.

The rest of the paper is organized as follows: in Sec. II, we review salient aspects of the generic nearest-neighbor anisotropic bilinear model on the pyrochlore lattice and briefly summarize the results that follow. In Sec. III, we present the irreducible representation analysis of the spin Hamiltonian and show how this can be used to derive the underlying gauge fields and emergent Gauss’s laws characterizing the various classical spin liquid phases of the model. Using this procedure, we identify in Sec. IV and V the regions in parameter space where both known as well as, to the best of our knowledge, heretofore unidentified classical spin liquid phases are realized. In Sec. VI, we show how the spin liquid regions in the  $\{J_{zz}, J_{\pm}, J_{\pm\pm}, J_{z\pm}\}$  phase diagram may intersect each other, and ultimately show that all the classical spin liquids in the most general nearest-neighbor Hamiltonian can be continuously connected, with no intermediate symmetry-broken phase bisecting them. Then, in Sec. VII, we provide numerical evidence for the stability in the limit  $T \rightarrow 0$  of these unexplored spin liquids identified in Sec. V. Finally, we conclude the paper in Sec. IX with a general overview of our results and perspective for future work.

## II. THE MODEL AND SUMMARY OF MAIN RESULTS

### A. The nearest neighbor pyrochlore model

This section summarizes the pyrochlore spin model, the location of classical spin liquids (CSLs) on its ground state phase diagram, and the emergent Gauss’s law of CSLs for readers seeking a quick overview. For those interested in a deeper dive into the technicalities, subsequent sections provide a comprehensive exploration of the field theory and the details of the classical Monte Carlo (CMC) simulations.

A prominent family of magnetic pyrochlore materials are the rare-earth pyrochlore oxides  $R_2M_2O_7$  [Fig. 1]. In

TABLE I. Table of all classical spin liquids (CSLs) for pyrochlore spin system with nearest-neighbor interaction [Eq.(1)]. The third column shows which coefficients are minimal in Eq. (13). The corresponding irreducible representation order parameters become the electric field constrained to generalized Gauss's laws. The fourth column shows the corresponding parameters in Eq. (1), and the fifth column shows the dimension of the parameter space (the overall scaling of all parameters is not considered). The sixth column lists the corresponding generalized Gauss's laws of the CSLs, whose derivation is discussed in detail of this work. The seventh column lists relevant references for previously known CSLs.

NON-KRAMERS CLASSICAL SPIN LIQUIDS						
	type and name	minimal irreps	coefficients	phase dim.	Gauss's laws	Refs.
1	Single R1U1 (Spin ice)	$\mathbb{T}_{1,i}$	$J_{zz} > 0$ $-J_{zz} < -6J_{\pm\pm}$ and $2J_{\pm\pm} \pm 4J_{\pm\pm}$	2D	$\nabla \cdot \mathbf{E}^{\text{ice}} = 0$	[17]
2	Double R1U1 ( $\text{SL}_{\perp}$ )	$\mathbb{T}_{1,p}, \mathbb{T}_2$	$J_{\pm\pm} = 0, J_{\pm} < 0$ $2J_{\pm} < 3J_{zz}$ and $-J_{zz}$	1D	$\nabla \cdot \mathbf{E}^A = 0$ $\nabla \cdot \mathbf{E}^B = 0$	[60]
3	Triple R1U1 (pHAF)	$\mathbb{T}_{1,i}, \mathbb{T}_{1,p}, \mathbb{T}_2$	$J_{zz} > 0$ $J_{zz} : J_{\pm} : J_{\pm\pm} = 2 : -1 : 0$	0D	$\partial_i E_{ij}^{\text{pHAF}} = 0$	[58, 60]
4	R1U1-R2U1 ( $\text{R}_1\text{-R}_2^{\mathbb{T}_1}$ )	$\mathbb{T}_{1,i}, \mathbf{E}, \mathbb{T}_{1,p}$	$J_{zz} > 0$ $J_{zz} : J_{\pm} : J_{\pm\pm} = 6 : 1 : -2$	0D	$\nabla \cdot \mathbf{E}^{\text{ice}} = 0$ $\partial_i E_{ij}^{\mathbb{T}_1+\mathbf{E}} = 0$	[62]
5	R1U1-R2U1 ( $\text{R}_1\text{-R}_2^{\mathbb{T}_2}$ )	$\mathbb{T}_{1,i}, \mathbf{E}, \mathbb{T}_2$	$J_{zz} > 0$ $J_{zz} : J_{\pm} : J_{\pm\pm} = 6 : 1 : 2$	0D	$\nabla \cdot \mathbf{E}^{\text{ice}} = 0$ $\partial_i E_{ij}^{\mathbb{T}_2+\mathbf{E}} = 0$	[62]
KRAMERS CLASSICAL SPIN LIQUIDS						
6	SV-R2U1 (SV $\equiv$ Scalar-vector)	$\mathbb{T}_{1,-}, \mathbf{E}, \mathbb{T}_2$	$J_{z\pm} > 0$ , Eq. (50)	1D	$ e^{ijk}  \partial_i E_{jk}^{\text{SV}} = 0$ $\partial_i E_{ij}^{\text{SV}} = 0$	
7	SV-R2U1* (Pinch-line spin liquid)	$\mathbb{T}_{1,-}, \mathbf{E}, \mathbb{T}_2$	$J_{z\pm} < 0$ , Eq. (50)	1D	$ e^{ijk}  \partial_i E_{jk}^{\text{SV}} = 0$ $\partial_i E_{ij}^{\text{SV}} = 0$	[61]
8	Triple R1U1 (HAFM)	$\mathbb{T}_{1,-}, \mathbf{E}, \mathbb{T}_2, \mathbf{A}_2$	$J_{zz} : J_{\pm} : J_{\pm\pm} : J_{z\pm}$ $= -2 : 1 : 2 : 2\sqrt{2}$	0D	$\partial_i E_{ij}^{\text{HAF}} = 0$	[58]
9	Triple R1U1 (HAFM*)	$\mathbb{T}_{1,-}, \mathbf{E}, \mathbb{T}_2, \mathbf{A}_2$	$J_{zz} : J_{\pm} : J_{\pm\pm} : J_{z\pm}$ $= -2 : 1 : 2 : -2\sqrt{2}$	0D	$\partial_i E_{ij}^{\text{HAF}} = 0$	

these materials, it is often the case that a strong crystal electric field (CEF) separates a ground state doublet from the rest of the single-ion spectrum, with a gap much larger than the energy scale of interactions [74, 75]<sup>2</sup>.

In such a scenario, it is convenient to describe these doublets as pseudospin-1/2 degrees of freedom (DOFs),  $S_i^\alpha$ , and to model the ion-ion superexchange interactions as interactions between these pseudospins [16, 27, 77–80].

The allowed form of nearest-neighbor interactions can then be determined by symmetry. When doing this, one must remember that the transformation of the pseudospins under lattice symmetries and time-reversal depends on the symmetry of the wave functions making up the CEF doublet. Through this analysis, three cases can

be distinguished: ‘dipolar’ Kramers in which the pseudospin transforms like an ordinary spin-1/2, ‘dipolar-octupolar’ Kramers in which one component of the pseudospin transforms like a magnetic octupole, and the non-Kramers case where two components transform like electric quadrupole moments (see Table 1 of Ref. [16]).

In general, the nearest-neighbor Hamiltonian may be written as follows

$$\begin{aligned}
 H_{\text{ex}} = \sum_{\langle ij \rangle} & \left[ J_{zz} S_i^z S_j^z - J_{\pm} (S_i^+ S_j^- + S_i^- S_j^+) \right. \\
 & + J_{\pm\pm} (\gamma_{ij} S_i^+ S_j^+ + \gamma_{ij}^* S_i^- S_j^-) \\
 & \left. - J_{z\pm} (\gamma_{ij}^* S_i^z S_j^+ + \gamma_{ij} S_i^z S_j^- + i \leftrightarrow j) \right], \quad (1)
 \end{aligned}$$

where  $S_i^z$  is the component of the spin directed along the local  $C_3$  symmetry axis (parallel to the local [111] cubic axis) at each site, and  $S_i^\pm$  are raising and lowering operators defined relative to that axis, and  $\gamma_{ij}$  are bond-

<sup>2</sup> The Tb-based pyrochlores [16, 30] and, to a lesser extent, the Er-based ones [76, 77] are examples where this crystal-field energy gap is fairly smaller.

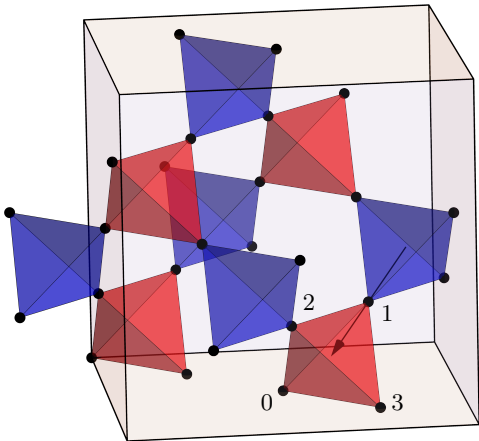


FIG. 1. Pyrochlore lattice where the spin degrees of freedom (DOFs) are located at the corners of the tetrahedra. We color the  $A$  and  $B$  tetrahedra in red and blue, respectively. Additionally, we illustrate the sublattice labels for the four sites of a single  $A$  tetrahedron along with the local  $z$  direction of the spin in sublattice 1 connecting the center of the adjacent tetrahedra sharing this lattice site.

dependent phase factors which depend on the nature of the low energy CEF doublet [16, 32, 52, 79]. For the dipolar Kramers [16, 52] and non-Kramers cases [16, 32, 78], the  $\gamma_{ij}$  phase factors take on values

$$\gamma = \begin{pmatrix} 0 & 1 & c & c^* \\ 1 & 0 & c^* & c \\ c & c^* & 0 & 1 \\ c^* & c & 1 & 0 \end{pmatrix}, \quad (2)$$

where  $c = e^{2\pi i/3}$ . For dipolar-octupolar pyrochlores  $\gamma_{ij} = 1$  on all bonds [16, 36, 38, 79]. Additionally, we note that for Kramers ions all components of the pseudospin are odd under time-reversal, while for non-Kramers ions the transverse components are time reversal even. This has the important consequence that  $J_{z\pm} = 0$  for non-Kramers ions [32, 78]. In the so-called dipolar-octupolar doublet systems, such as in the pyrochlores with  $\text{Ce}^{3+}$ ,  $\text{Sm}^{3+}$  and  $\text{Nd}^{3+}$  rare-earth ions<sup>3</sup>, the  $\gamma_{ij}$  phase factors are  $\gamma_{ij} = 1$  on all nearest-neighbor bonds.

In a classical description of Eq. (1) we replace the  $S^\pm$  operators with  $S^x \pm iS^y$  and treat  $\mathbf{S} = (S^x, S^y, S^z)$  as an  $O(3)$  vector of fixed length  $S$ . Moreover, within a classical description, or within the context of materials with a larger spin value [81], it becomes meaningful to consider a single ion anisotropy term, whose simplest uniaxial form can be added to  $H_{\text{ex}}$ :

$$H = H_{\text{ex}} + H_{\text{si}}, \quad H_{\text{si}} = D \sum_i (S_i^z)^2 \quad (3)$$

<sup>3</sup> The classical  $\text{Dy}_2(\text{Ti}, \text{Sn}, \text{Ge})_2\text{O}_7$  spin ices [28] with magnetic  $\text{Dy}^{3+}$  are also dipolar-octupolar materials, albeit with rather small non-Ising  $J_{zz}$  couplings in Eq. (1) [27]

In this work, we set the single-ion terms to be zero and focus on the  $H_{\text{ex}}$  terms only. Although we consider this simplified case, our field theory analysis could be straightforwardly generalized to the case with non-zero  $H_{\text{si}}$  terms. We note that the results presented in this work focus on the classical Kramers and non-Kramers Hamiltonians, as the classical and quantum phase diagrams of the the DO Hamiltonian have already been studied in detail in previous work [36, 38].

## B. Main results

We comprehensively analyze the parameter space  $\{J_{zz}, J_\pm, J_{\pm\pm}, J_{z\pm}\}$  for the classical dipolar spin system to map out *all* classical spin liquids in the phase diagram by combining analytical theory with classical Monte Carlo (CMC) simulations. Analytically, we construct a long-wavelength field theory based on inter-tetrahedron constraints, unveiling various generalized Gauss's law that characterizes the degenerate ground states of different CSLs. This theoretical framework proves exact in the limit of a large number of spin components  $\mathcal{N}$ . Through CMC simulations, we verify that the three component spin models (henceforth referred to as Heisenberg spin models) remain disordered down to the lowest temperatures examined, and then further investigate the system's thermodynamic properties and correlations. We note that the existence of an emergent Gauss's law from the large- $\mathcal{N}$  field theory is a necessary but not sufficient condition for the Heisenberg spin CSLs – there are cases in which the large- $\mathcal{N}$  theory predicts a CSL but the Heisenberg spin model orders at low temperatures eventually [82]. Such cases are usually associated with a thermal order-by-disorder selection [13, 69, 83–85] which are typically associated with higher-order terms in a free energy descriptions which are not included in the large- $\mathcal{N}$  analysis [62].

We have identified a total of *nine* classical spin liquids (CSLs). The parameter spaces they occupy and their corresponding emergent Gauss's laws are detailed in Table I. The generalized Gauss's laws include the conventional Maxwell Gauss's law, i.e., charge as the divergence of a vector field, as well as more exotic forms such as coexisting two or three copies of Maxwell Gauss's law, charges defined by rank-2 matrix electric field, and a mixture of them. In this table, we use a naming convention for the spin liquids based on the structure of emergent gauge fields describing the low-temperature physics (R1  $\equiv$  rank-1 or R2  $\equiv$  rank-2), the gauge structure constraining the field (this being U1  $\equiv$  U(1) for all the CSLs described in the present work), and then provide in parenthesis the name these CSLs were given (if there exist any) when first identified [17, 58, 60–62]. For example, for the spin ice CSL, the low-energy theory is described by a single rank-1 (R1) field with a U(1) (U1) structure characterized by the emergent Gauss's law on the rank-1 field. In our notation this is the single R1U1 (spin ice) spin liquid.

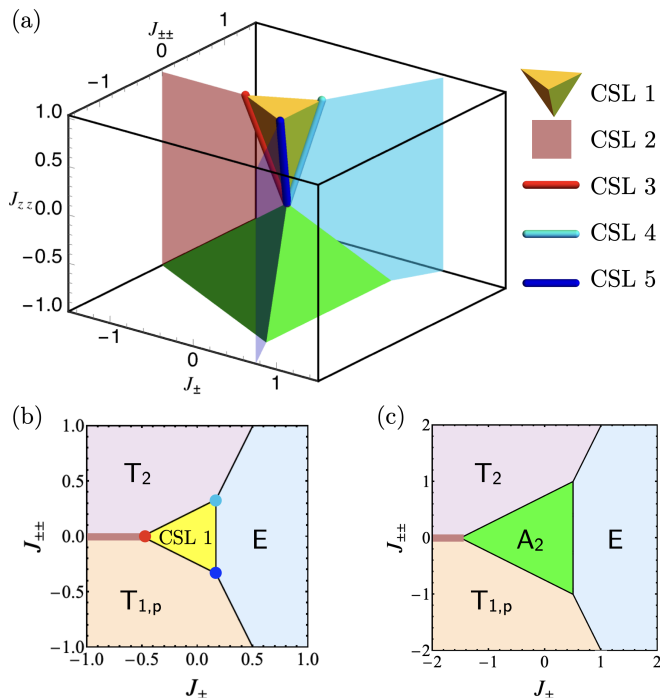


FIG. 2. (a) Phase diagram of classical spin liquids (CSLs) for the non-Kramers Hamiltonian [Sec. IV]. There are five CSLs in the phase diagram. CSL 1 (spin ice) occupies a 3D volume, CSL 2 occupies a surface, and the other three CSLs occupy different lines. (b) Cross-section of the phase diagram at  $J_{zz} = 1$ , showing all five CSLs. The irreducible representations of the magnetic ordered phases are also labeled. (c) cross-section at  $J_{zz} = -1$ . Only CSL 2 lives in this part of the phase diagram.

The four-dimensional phase diagram can be qualitatively divided into two regions based on the value of  $J_{z\pm}$ : one where  $J_{z\pm} = 0$  (appropriate to non-Kramers materials), illustrated in Fig. 2, and another where  $J_{z\pm} \neq 0$ , illustrated in Fig. 3. Different CSLs are found within these distinct phase diagrams. The CSLs labeled 1 to 5 live on the phase diagram of  $J_{z\pm} = 0$  while CSLs 6 to 9 live on the phase diagram of  $J_{z\pm} \neq 0$ . Except for spin ice (CSL 1), all other CSLs reside on the phase boundaries of magnetic orders. However, not all phase boundaries separating long-range magnetic orders host CSLs.

Among the nine identified CSLs, many of them, such as the extensively investigated spin ice and the Heisenberg antiferromagnetic (HAFM) model, have been individually explored in prior research. However, this study is the first to make a comprehensive study of their effective field theory, phase diagram, and transitions among different CSLs. Notably, the CSLs 6 and 9 have not been identified in previous literature. We will discuss below the properties of these CSLs in detail.

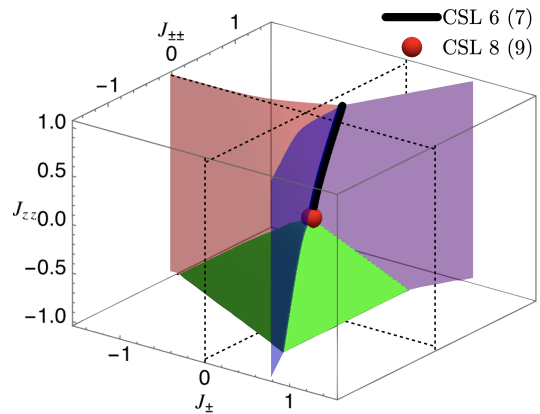


FIG. 3. Phase diagram of classical spin liquids (CSLs) for the Kramers Hamiltonian [Sec. V]. CSL 6 and 8 are realized in this phase diagram (here,  $J_{z\pm}$  was taken to be 0.1). The CSL 6 is the scalar-vector rank-2 U(1) spin liquid, and occupies the black line. CSL 8 is the Heisenberg antiferromagnet, corresponding to the red dot. By taking  $J_{z\pm} = -0.1$ , the shape of the phase diagram remains the same, but CSL 6 becomes CSL 7 and CSL 8 becomes CSL 9.

### III. THE IRREPS AND INTER-TETRAHEDRON CONSTRAINTS

#### A. Diagonalization of the single tetrahedron Hamiltonian

Every nearest-neighbor bond in the pyrochlore lattice belongs uniquely to one tetrahedron ( $A$  or  $B$  in Fig 1). The nearest-neighbor Hamiltonian, can therefore be expressed as a sum of terms over individual tetrahedra [53] which include a spin-spin exchange interaction term,  $H_{\text{ex}}(t)$  and, for generality sake, a single-ion term,  $H_{\text{si}}(t)$ , each acting on each individual tetrahedron  $t$ .

$$H = \sum_t H_t, \quad H_t = H_{\text{ex}}(t) + \frac{1}{2} H_{\text{si}}(t), \quad (4)$$

where  $H_{\text{ex}}(t)$  and  $H_{\text{si}}(t)$  are the exchange and single-ion Hamiltonians acting on a single tetrahedron,  $t$ . Here, the factor of  $1/2$  arises to avoid double counting of the single ion term, since sites are shared by two tetrahedra.

The single tetrahedron Hamiltonian  $H_t$  can then be re-expressed as a sum of quadratic terms:

$$H_t = a_{A_2} m_{A_2}^2 + a_E m_E^2 + a_{T_2} m_{T_2}^2 + (a_{T_{1,i}} m_{T_{1,i}}^2 + a_{T_{1,p}} m_{T_{1,p}}^2 + a_{T_{1,ip}} \mathbf{m}_{T_{1,i}} \cdot \mathbf{m}_{T_{1,p}}), \quad (5)$$

where each  $\mathbf{m}_\chi$  is a local order parameter for different kinds of magnetic configuration corresponding to a particular irreducible representation (irrep) of  $T_d$ , the symmetry group of a tetrahedron, see Fig. 4.

We use  $\mathbf{m}_\chi$  to represent both the vector  $\mathbf{m}_\chi$  irreps and scalar  $m$  irreps for simplicity of notation. Each  $\mathbf{m}_\chi$  is defined as a specific linear combination of the spin components which are given in Table II. The labels

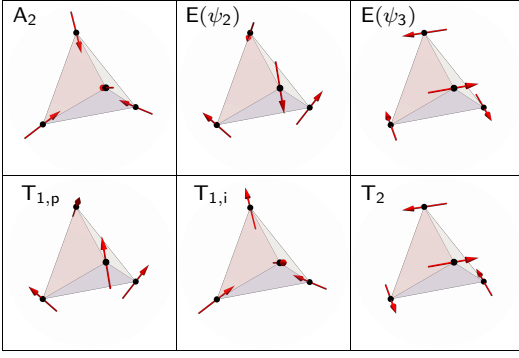


FIG. 4. Spin configuration of the irreducible representation configurations.

$A_2, E, T_1, T_2$  correspond to different irreps of the point group of a tetrahedron, according to which the different  $m$  or  $\mathbf{m}_X$  fields transform. The coefficients  $a_X$  are linear combinations of the exchange interaction parameters  $J_{zz}, J_{\pm}, J_{\pm\pm}, J_{z\pm}$  and the single-ion anisotropy  $D$ , as listed in Table III.

The coupling term between  $\mathbf{m}_{T_{1,i}}$  and  $\mathbf{m}_{T_{1,p}}$ , which each transform according to  $T_1$ , can be removed by a parameter-dependent redefinition of the fields. We define:

$$\mathbf{m}_{T_{1,-}} = \cos \phi \mathbf{m}_{T_{1,i}} + \sin \phi \mathbf{m}_{T_{1,p}}, \quad (6)$$

$$\mathbf{m}_{T_{1,+}} = -\sin \phi \mathbf{m}_{T_{1,i}} + \cos \phi \mathbf{m}_{T_{1,p}}, \quad (7)$$

where

$$\mathbf{v}_- = \begin{pmatrix} v_{i-} \\ v_{p-} \end{pmatrix} \equiv \begin{pmatrix} \cos \phi \\ \sin \phi \end{pmatrix}, \quad (8)$$

$$\mathbf{v}_+ = \begin{pmatrix} v_{i+} \\ v_{p+} \end{pmatrix} \equiv \begin{pmatrix} -\sin \phi \\ \cos \phi \end{pmatrix}, \quad (9)$$

are the normalized eigenvectors of the  $2 \times 2$  matrix

$$\begin{pmatrix} a_{T_{1,i}} & \frac{1}{2}a_{T_{1,ip}} \\ \frac{1}{2}a_{T_{1,ip}} & a_{T_{1,p}} \end{pmatrix},$$

with eigenvalues

$$a_{T_{1,-}} = \frac{1}{2}(a_{T_{1,i}} + a_{T_{1,p}} - \sqrt{(a_{T_{1,i}} - a_{T_{1,p}})^2 + a_{T_{1,ip}}^2}), \quad (10)$$

$$a_{T_{1,+}} = \frac{1}{2}(a_{T_{1,i}} + a_{T_{1,p}} + \sqrt{(a_{T_{1,i}} - a_{T_{1,p}})^2 + a_{T_{1,ip}}^2}), \quad (11)$$

respectively. Here,  $\phi$  corresponds to the mixing angle between  $\mathbf{m}_{T_{1,p}}$  and  $\mathbf{m}_{T_{1,i}}$  due to non-zero  $J_{z\pm}$ ,

$$\phi = \frac{1}{2} \arctan \left( \frac{a_{T_{1,ip}}}{a_{T_{1,i}} - a_{T_{1,p}}} \right). \quad (12)$$

With this redefinition of the  $T_1$  fields, the diagonalized Hamiltonian for a single tetrahedron becomes:

$$H_t = a_{A_2} m_{A_2}^2 + a_E m_E^2 + a_{T_2} m_{T_2}^2 + a_{T_{1,-}} m_{T_{1,-}}^2 + a_{T_{1,+}} m_{T_{1,+}}^2, \quad (13)$$

the sum of the squares of the  $\mathbf{m}_X$  fields is constrained as a result of the spin normalization:

$$m_{A_2}^2 + m_E^2 + m_{T_2}^2 + m_{T_{1,-}}^2 + m_{T_{1,+}}^2 = 4S^2 \quad (14)$$

where  $S \equiv |\mathbf{S}|$  is the spin length. It is particularly useful to identify which term in Eq. (13) has the lowest coefficient  $a_X$ 's and remove them (there could be one or more  $a_X$  being minimal) by using Eq. (14).

Defining:

$$\mathcal{E}_0 \equiv \min(a_{A_2}, a_E, a_{T_2}, a_{T_{1,-}}, a_{T_{1,+}}), \quad (15)$$

we then add and subtract  $4\mathcal{E}_0 S^2$  from Eq. (13) and use Eq. (14) to obtain:

$$H_t = (a_{A_2} - \mathcal{E}_0) m_{A_2}^2 + (a_E - \mathcal{E}_0) m_E^2 + (a_{T_2} - \mathcal{E}_0) m_{T_2}^2 + (a_{T_{1,-}} - \mathcal{E}_0) m_{T_{1,-}}^2 + (a_{T_{1,+}} - \mathcal{E}_0) m_{T_{1,+}}^2 + 4S^2 \mathcal{E}_0. \quad (16)$$

Each multiplicative prefactor in Eq. (16) is either vanishing (where  $a_X = \mathcal{E}_0$ ) or strictly positive. From that equation, we can directly read off the ground state constraints for any  $\{J_{zz}, J_{\pm}, J_{\pm\pm}, J_{z\pm}, D\}$  parameter set:

$$\sum_X m_X^2 = 1 \text{ for } X \text{ such that } a_X = \mathcal{E}_0; \quad (17)$$

$$m_Y = 0 \forall Y \text{ such that } a_Y > \mathcal{E}_0. \quad (18)$$

These constraints are applied to every tetrahedron  $t$ . In the  $T \rightarrow 0$  limit, the components of the  $X$  irreps are free to fluctuate and these therefore correspond to the fluctuating DOFs at low  $T$ . On the other hand, the  $Y$  irreps become ultimately frozen and introduce constraints on the ground state configurations. If there are enough DOFs among the  $\mathbf{m}_X$  fields, then the first condition [Eq. (17)] does not pin down the value of each  $\mathbf{m}_X$  or induce magnetic order. In such a case, we may treat  $\mathbf{m}_X$ 's as almost freely fluctuating at the level of a single tetrahedron. Equation (18) will be used in combination with the inter-tetrahedron constraints, to ultimately understand the Gauss's laws that emerge in the system and control the ground state.

## B. Inter-tetrahedron constraints and coarse-graining

Equation (18) establishes a generalized set of constraints which, in a ground state, must be fulfilled on every tetrahedron of the lattice. The problem of fulfilling these constraints is rendered nontrivial by the fact that the constraints are not fully independent: neighboring tetrahedra share a spin. So the ground state condition on one tetrahedron, say of type  $A$ , must also be respected by its neighboring tetrahedra, say of type  $B$ .

To understand the consequences of this, it is useful to divide the pyrochlore tetrahedra into two sets,  $A$  and  $B$ ,

TABLE II. Local order parameters  $\mathbf{m}_x$  as irreducible representation (irrep) of  $T_d$ , the symmetry group of a tetrahedron. The first column is the corresponding symmetry operation. The second column gives the corresponding magnetic phases. The third column lists the order parameter defined in terms of spins.

Symmetry	Phase	Order parameter
$A_{2g} (\Gamma_3)$	all-in/all-out	$m_{A_2} = S_1^z + S_2^z + S_3^z + S_4^z$
$E_g (\Gamma_5)$	$\psi$ phase	$\mathbf{m}_E = \begin{pmatrix} S_1^x + S_2^x + S_3^x + S_4^x \\ S_1^y + S_2^y + S_3^y + S_4^y \end{pmatrix}$
$T_{2g} (\Gamma_7)$	Palmer-Chalker	$\mathbf{m}_{T_2} = \begin{pmatrix} S_1^y + S_2^y - S_3^y - S_4^y \\ \left(-\frac{\sqrt{3}}{2}S_1^x - \frac{1}{2}S_1^y\right) - \left(-\frac{\sqrt{3}}{2}S_2^x - \frac{1}{2}S_2^y\right) + \left(-\frac{\sqrt{3}}{2}S_3^x - \frac{1}{2}S_3^y\right) - \left(-\frac{\sqrt{3}}{2}S_4^x - \frac{1}{2}S_4^y\right) \\ \left(\frac{\sqrt{3}}{2}S_1^x - \frac{1}{2}S_1^y\right) - \left(\frac{\sqrt{3}}{2}S_2^x - \frac{1}{2}S_2^y\right) - \left(\frac{\sqrt{3}}{2}S_3^x - \frac{1}{2}S_3^y\right) + \left(\frac{\sqrt{3}}{2}S_4^x - \frac{1}{2}S_4^y\right) \end{pmatrix}$
$T_{1g} (\Gamma_9)$	spin ice	$\mathbf{m}_{T_{1,i}} = \begin{pmatrix} S_1^z + S_2^z - S_3^z - S_4^z \\ S_1^z - S_2^z + S_3^z - S_4^z \\ S_1^z - S_2^z - S_3^z + S_4^z \end{pmatrix}$
$T'_{1g} (\Gamma_9)$	splayed ferromagnet	$\mathbf{m}_{T_{1,p}} = \begin{pmatrix} S_1^x + S_2^x - S_3^x - S_4^x \\ \left(-\frac{1}{2}S_1^x + \frac{\sqrt{3}}{2}S_1^y\right) - \left(-\frac{1}{2}S_2^x + \frac{\sqrt{3}}{2}S_2^y\right) + \left(-\frac{1}{2}S_3^x + \frac{\sqrt{3}}{2}S_3^y\right) - \left(-\frac{1}{2}S_4^x + \frac{\sqrt{3}}{2}S_4^y\right) \\ -\frac{1}{2}S_1^x - \frac{\sqrt{3}}{2}S_1^y - \left(-\frac{1}{2}S_2^x - \frac{\sqrt{3}}{2}S_2^y\right) - \left(-\frac{1}{2}S_3^x - \frac{\sqrt{3}}{2}S_3^y\right) + \left(-\frac{1}{2}S_4^x - \frac{\sqrt{3}}{2}S_4^y\right) \end{pmatrix}$

TABLE III. Coefficients of the irreducible representations in Eq. (5) in terms of exchange parameters in Eq. (1).

Coefficient	Definition in terms of exchange parameters $\{J_{zz}, J_{\pm}, J_{\pm\pm}, J_{z\pm}, D\}$
$a_{A_2}$	$3J_{zz} + D$
$a_E$	$-6J_{\pm}$
$a_{T_2}$	$2J_{\pm} - 4J_{\pm\pm}$
$a_{T_{1,i}}$	$-J_{zz} + D$
$a_{T_{1,p}}$	$2J_{\pm} + 4J_{\pm\pm}$
$a_{T_{1,ip}}$	$-8J_{z\pm}$

such that the neighbors of an  $A$  tetrahedron are all  $B$  tetrahedra and vice versa, see Fig. 1. The centers of the  $A$  and  $B$  tetrahedra each form a pair of face-centered cubic (FCC) lattices, the two types together forming a diamond lattice.

One can then place the  $A$  tetrahedra into ground state configurations independently, since they do not overlap with each other. Specifying a ground state configuration on the  $A$  tetrahedra amounts to setting the values of all the  $\mathbf{m}_Y = 0$  according to the energetic constraint given by Eq. (18) (i.e. those for which  $a_Y > \mathcal{E}_0$ ), while freely choosing a certain combination of the other  $\mathbf{m}_X$  fields, up to spin normalization constraints. Since every spin is included in exactly one  $A$  tetrahedron, and since the map between  $\mathbf{m}$  fields and the spins is invertible, this construction completely determines the allowed spin

configurations in the  $A$  tetrahedra when these are taken independently.

However,  $\mathbf{m}_X$ 's on  $A$  tetrahedra have an additional constraint. In order to be a ground state, the configurations must also satisfy the constraints on the  $B$  tetrahedra. The requirement on  $B$  tetrahedra constrains the  $\mathbf{m}_X$  fields on the four  $A$  tetrahedra surrounding it. The mutual constraint between the  $A$  and  $B$  tetrahedra can be seen more clearly by writing the four spins belonging to the  $B$  tetrahedron in terms of the values of the  $\mathbf{m}_X$  fields on the four surrounding  $A$  tetrahedra. Using the relationship between the  $B$  tetrahedron and the  $A$   $\mathbf{m}_X$  fields, the constraint on the  $\mathbf{m}_X$ 's on the  $B$  tetrahedra can be expressed in terms of the fields on the surrounding  $A$  tetrahedra. On each  $B$  tetrahedron, one obtains a set of equations of the following general form:

$$\begin{aligned}
\mathbf{m}_Y(\mathbf{R}_B) &= 0 \\
\implies \sum_{i=1}^4 \sum_{X \in \text{gs}} \sum_{\alpha} c_{i\alpha X} m_X^{\alpha}(\mathbf{R}_B + \mathbf{u}_i) &= 0 \quad (19) \\
\stackrel{\text{coarse-grained}}{\longrightarrow} \sum_{X \in \text{gs}} \sum_{\alpha} D_{i\alpha X} m_X^{\alpha} &= 0,
\end{aligned}$$

where, on the second line, the  $\mathbf{u}_i$ 's are the FCC vectors connecting the center of each  $B$  tetrahedron to the centers of the four neighboring  $A$  tetrahedra. The sum taken over the  $X$  irreps is performed over those fields in the  $A$  tetrahedra which are not constrained to be zero by Eq. (18). The sums over  $\alpha$  runs over each component of each  $\mathbf{m}_X^{\alpha}$ , and the  $c_{i\alpha X}$ 's are constant coefficients obtained by relating the  $B$  tetrahedra  $\mathbf{m}_X$  fields to those on the  $A$

tetrahedra, and  $D_{i\alpha\chi}$  is a generalized set of derivatives. The  $c_{i\alpha\chi}$  coefficients and the explicit form of the  $D_{i\alpha\chi}$  derivatives can be worked out using the linear relations between the fields  $\mathbf{m}_\chi$  and the spins  $\mathbf{S}$ : a spin  $\mathbf{S}_i$  shared by two adjacent  $A$  and  $B$  tetrahedra is written in terms of the  $\mathbf{m}(\mathbf{R}_B)$  of the  $B$  tetrahedra, i.e.  $\mathbf{S}_i[\mathbf{m}(\mathbf{R}_B)]$ . Then, using the definition of the  $\mathbf{m}(\mathbf{R}_A)$  fields for the  $A$  tetrahedron provided in Table II, a relationship between the fields on the  $A$  and  $B$  tetrahedra is obtained. We note that the most interesting form of these relations arises in the coarse-grained limit, which we further discuss below, at the end of Sec. III C, and where we provide the simplest example of the derivation of these equations.

We note that the constraints in Eq. (19) on the ground state configuration yield a set of differential equations on the  $\mathbf{m}_\chi$  fields. These constraints can be expressed into a form reminiscent of a Gauss's law upon which we can then apply a coarse-graining procedure. In this procedure we assume, for each  $\mathbf{m}_\chi$ , the existence of some

underlying smoothly varying field  $\mathbf{m}_\chi(\mathbf{r})$  defined at all points in space (here we slightly abuse the notation to use  $\mathbf{m}_\chi$  to refer to both the irreps on the discrete lattice and the coarse-grained fields). We further suppose that if this smoothly varying field is evaluated at the center of an  $A$  tetrahedron, it has the value of  $\mathbf{m}_\chi$  on that tetrahedron center.

Then, assuming slow variations of the fields, we approximate  $m_\chi^\alpha(\mathbf{R}_B - \mathbf{u}_i)$  appearing in Eq. (19) by a low-order gradient expansion of  $\mathbf{m}_\chi(\mathbf{r})$  about  $\mathbf{r} = \mathbf{R}_B$ . Keeping the lowest order terms in the resulting expansion of Eq. (19) establishes the effective Gauss's law(s) governing the long-wavelength fluctuations of the ground state fields.

Working through this procedure yields the following set of correspondences between microscopic constraints on the  $B$  tetrahedra and constraints on the derivatives of the coarse-grained fields:

$$m_{A_2} = 0 \implies m_{A_2} = -\frac{a_d}{\sqrt{3}} \sin \phi \nabla \cdot \mathbf{m}_{T_{1,+}} + \frac{a_d}{\sqrt{3}} \cos \phi \nabla \cdot \mathbf{m}_{T_{1,-}} = 0, \quad (20)$$

$$\begin{aligned} \mathbf{m}_E = 0 \implies \mathbf{m}_E &= \frac{a_d}{2\sqrt{3}} \cos \phi \begin{pmatrix} 2\partial_x m_{T_{1,+}}^x - \partial_y m_{T_{1,+}}^y - \partial_z m_{T_{1,+}}^z \\ \sqrt{3}(\partial_y m_{T_{1,+}}^y - \partial_z m_{T_{1,+}}^z) \end{pmatrix} + \frac{a_d}{2\sqrt{3}} \sin \phi \begin{pmatrix} 2\partial_x m_{T_{1,-}}^x - \partial_y m_{T_{1,-}}^y - \partial_z m_{T_{1,-}}^z \\ \sqrt{3}(\partial_y m_{T_{1,-}}^y - \partial_z m_{T_{1,-}}^z) \end{pmatrix} \\ &+ \frac{a_d}{2\sqrt{3}} \begin{pmatrix} \sqrt{3}(\partial_z m_{T_2}^z - \partial_y m_{T_2}^y) \\ 2\partial_x m_{T_2}^x - \partial_y m_{T_2}^y - \partial_z m_{T_2}^z \end{pmatrix} = 0, \end{aligned} \quad (21)$$

$$\mathbf{m}_{T_2} = 0 \implies \mathbf{m}_{T_2} = \frac{a_d}{2\sqrt{3}} \begin{pmatrix} 2\partial_x m_E^2 \\ -\sqrt{3}\partial_y m_E^1 - \partial_z m_E^2 \end{pmatrix} + \frac{a_d}{2} \cos \phi \nabla \times \mathbf{m}_{T_{1,+}} + \frac{a_d}{2} \sin \phi \nabla \times \mathbf{m}_{T_{1,-}} = 0, \quad (22)$$

$$\begin{aligned} \mathbf{m}_{T_{1,-}} = 0 \implies \mathbf{m}_{T_{1,-}} &= \frac{a_d}{\sqrt{3}} \cos \phi \nabla m_{A_2} + \frac{\sqrt{3}a_d}{2} \sin \phi \cos \phi \begin{pmatrix} \partial_y m_{T_{1,+}}^z + \partial_z m_{T_{1,+}}^y \\ \partial_z m_{T_{1,+}}^x + \partial_x m_{T_{1,+}}^z \\ \partial_x m_{T_{1,+}}^y + \partial_y m_{T_{1,+}}^x \end{pmatrix} \\ &+ \frac{a_d}{2\sqrt{3}} \sin \phi \begin{pmatrix} 2\partial_x m_E^1 \\ -\partial_y m_E^1 + \sqrt{3}\partial_y m_E^2 \\ -\partial_z m_E^1 - \sqrt{3}\partial_z m_E^2 \end{pmatrix} + \frac{a_d}{2} \sin \phi \nabla \times \mathbf{m}_{T_2} = 0, \end{aligned} \quad (23)$$

$$\begin{aligned} \mathbf{m}_{T_{1,+}} = 0 \implies \mathbf{m}_{T_{1,+}} &= -\frac{a_d}{\sqrt{3}} \sin \phi \nabla m_{A_2} - \frac{\sqrt{3}a_d}{2} \sin \phi \cos \phi \begin{pmatrix} \partial_y m_{T_{1,-}}^z + \partial_z m_{T_{1,-}}^y \\ \partial_z m_{T_{1,-}}^x + \partial_x m_{T_{1,-}}^z \\ \partial_x m_{T_{1,-}}^y + \partial_y m_{T_{1,-}}^x \end{pmatrix} \\ &+ \frac{a_d}{2\sqrt{3}} \cos \phi \begin{pmatrix} 2\partial_x m_E^1 \\ -\partial_y m_E^1 + \sqrt{3}\partial_y m_E^2 \\ -\partial_z m_E^1 - \sqrt{3}\partial_z m_E^2 \end{pmatrix} + \frac{a_d}{2} \cos \phi \nabla \times \mathbf{m}_{T_2} = 0. \end{aligned} \quad (24)$$

Here,  $a_d$  is the lattice constant. Note that here, we have kept all the field  $\mathbf{m}_\chi$  on the right hand side of the equalities. In practice the Gauss's laws for a particular system are obtained by only considering the differential equations resulting from the frozen  $\mathbf{m}_\gamma$  fields on the left hand sides of Eq. (20)-(24) while only keeping terms involving the fluctuating  $\mathbf{m}_\chi$  fields on the right hand sides. In the next subsection we provide an example of this pro-

cedure for the classical spin ice spin liquid.

### C. The non-Kramers case

We start by considering the case of non-Kramers spins where the irrep analysis and inter-tetrahedron con-



straints take simpler forms. In this case,  $J_{z\pm} = 0$ , so that  $a_{\mathbb{T}_{1,p}} = 0$  (see Table III). As a consequence, the ir-

reps  $\mathbf{m}_{\mathbb{T}_{1,i}}$  and  $\mathbf{m}_{\mathbb{T}_{1,p}}$  do not mix. The inter-tetrahedron constraints then take a rather compact form

$$m_{A_2} = 0 \implies m_{A_2} = \frac{a_d}{\sqrt{3}} \nabla \cdot \mathbf{m}_{\mathbb{T}_{1,i}} = 0, \quad (25)$$

$$\mathbf{m}_{\mathbb{E}} = 0 \implies \mathbf{m}_{\mathbb{E}} = \frac{a_d}{2\sqrt{3}} \begin{pmatrix} 2\partial_x m_{\mathbb{T}_{1,p}}^x - \partial_y m_{\mathbb{T}_{1,p}}^y - \partial_z m_{\mathbb{T}_{1,p}}^z \\ \sqrt{3}(\partial_y m_{\mathbb{T}_{1,p}}^y - \partial_z m_{\mathbb{T}_{1,p}}^z) \end{pmatrix} + \frac{a_d}{2\sqrt{3}} \begin{pmatrix} \sqrt{3}(-\partial_y m_{\mathbb{T}_2}^y + \partial_z m_{\mathbb{T}_2}^z) \\ 2\partial_x m_{\mathbb{T}_2}^x - \partial_y m_{\mathbb{T}_2}^y - \partial_z m_{\mathbb{T}_2}^z \end{pmatrix} = 0, \quad (26)$$

$$\mathbf{m}_{\mathbb{T}_2} = 0 \implies \mathbf{m}_{\mathbb{T}_2} = \frac{a_d}{2\sqrt{3}} \begin{pmatrix} 2\partial_x m_{\mathbb{E}}^2 \\ -\sqrt{3}\partial_y m_{\mathbb{E}}^1 - \partial_y m_{\mathbb{E}}^2 \\ \sqrt{3}\partial_z m_{\mathbb{E}}^1 - \partial_z m_{\mathbb{E}}^2 \end{pmatrix} + \frac{a_d}{2} \nabla \times \mathbf{m}_{\mathbb{T}_{1,p}} = 0, \quad (27)$$

$$\mathbf{m}_{\mathbb{T}_{1,i}} = 0 \implies \mathbf{m}_{\mathbb{T}_{1,i}} = \frac{a_d}{\sqrt{3}} \nabla m_{A_2} = 0, \quad (28)$$

$$\mathbf{m}_{\mathbb{T}_{1,p}} = 0 \implies \mathbf{m}_{\mathbb{T}_{1,p}} = \frac{a_d}{2\sqrt{3}} \begin{pmatrix} 2\partial_x m_{\mathbb{E}}^1 \\ -\partial_y m_{\mathbb{E}}^1 + \sqrt{3}\partial_y m_{\mathbb{E}}^2 \\ -\partial_z m_{\mathbb{E}}^1 - \sqrt{3}\partial_z m_{\mathbb{E}}^2 \end{pmatrix} + \frac{a_d}{2} \nabla \times \mathbf{m}_{\mathbb{T}_2} = 0. \quad (29)$$

Before proceeding, we note that for the non-Kramers Hamiltonian, the local  $z$  spin degrees of freedom transform as (time-odd) magnetic dipoles while the local  $xy$  spin degrees of freedom transform as (time-even) magnetic quadrupoles [32], which forbids a bilinear mixing of these degrees of freedom. This restriction is further reflected in Eq. (25)-(29) where each constraint results in a differential equation involving fields constructed by the local  $z$  spin degrees of freedom (the  $A_2$  and the  $\mathbb{T}_{1,i}$  fields) or by the local  $xy$  spin degrees of freedom (the  $\mathbb{E}$ , the  $\mathbb{T}_{1,i}$ , and the  $\mathbb{T}_2$  fields). This distinction allows us to further classify the constraints in Eq. (25)-(29) into two independent sets of constraints.

For illustration purposes, let us take Eq. (25) as an example to show how these field-theory constraints are derived. We label the four sublattice sites on the  $B$  tetrahedron to be 1, 2, 3, 4, and have

$$m_{A_2} = S_1^z + S_2^z + S_3^z + S_4^z. \quad (30)$$

The  $B$  tetrahedron is joined with the  $A$  tetrahedron along the [111] cubic direction by the spin  $\mathbf{S}_1$ . We see that on the  $A$  tetrahedron,  $S_1^z$  can be expressed as linear combinations of  $\mathbf{m}$  fields on the  $A$  tetrahedron as

$$S_1^z = \frac{1}{4} (m_{A_2} + [111] \cdot \mathbf{m}_{\mathbb{T}_{1,i}}). \quad (31)$$

Repeating a similar calculation for the other spins  $\mathbf{S}_{2,3,4}$  results in the follow expression relating  $m_{A_2}$  on a  $B$  tetrahedron,  $m_{A_2}(\mathbf{R}_B)$ , to the neighboring four  $A$  tetrahedra

$$m_{A_2}(\mathbf{R}_B) = \frac{1}{4} \sum_i \left( m_{A_2}(\mathbf{R}_B + \mathbf{u}_i) + \frac{a_d}{\sqrt{3}} \hat{\mathbf{u}}_i \cdot \mathbf{m}_{\mathbb{T}_{1,i}}(\mathbf{R}_B + \mathbf{u}_i) \right), \quad (32)$$

where  $a_d$  is the lattice constant (linear dimension of the cubic unit cell). Then, applying the constraint  $m_{A_2} =$

0 and taking the  $\mathbf{m}_{\mathbb{X}}$  fields to the continuous limit, we obtain

$$m_{A_2} = 0 \implies \nabla \cdot \mathbf{m}_{\mathbb{T}_{1,i}} = 0, \quad (33)$$

which gives Eq. (25). The other equations in Eqs. (20-24) and Eqs. (25-29) can be derived in the same fashion, by considering the other  $\mathbf{m}_{\mathbb{X}}$  fields on the left side of those equations one at a time, although the algebra is more lengthy.

#### D. Step-by-step procedure for deriving Gauss's law

We now use the irreps and inter-tetrahedron constraints to identify the CSLs that the model supports for non-Kramers ions. We consider all combinations of some coefficients  $a_{\mathbb{X}}$ 's being minimal and  $a_{\mathbb{Y}}$ 's not minimal in the single-tetrahedron Hamiltonian.

The field theory analysis recipe is then

- *Step #0:* Compute the  $a_{\mathbb{X}}$  coefficients for all irrep fields and identify all the minimum energy irreps for which  $a_{\mathbb{X}} = \mathcal{E}_0$  according to Eq. (15).
- *Step #1:* Then, identify all  $\mathbf{m}_{\mathbb{Y}} = 0$  as constrained by Eq. (18) which become frozen and are thermally depopulated in the limit  $T \rightarrow 0$ .
- *Step #2:* Then, identify all  $\mathbf{m}_{\mathbb{X}}$ 's that are allowed to fluctuate on a single tetrahedron and are free to fluctuate.
- *Step #3:* Next, identify the constraints on  $\mathbf{m}_{\mathbb{X}}$ 's, imposed by  $\mathbf{m}_{\mathbb{Y}} = 0$  through the inter-tetrahedron relations Eqs. (20-24) or Eqs. (25-29).

- *Step #4*: Finally, verify that in the large- $\mathcal{N}$  theory, the  $a_X$  parameters identified yield low-energy flat bands reflecting the extensive degeneracy characteristic of a classical spin liquid phase. The number of flat bands correspond to the number of DOFs in the emergent electric fields minus the number of constraints.

This procedure provides us with a list of all potential CSLs according to the large- $\mathcal{N}$  limit. Subsequently, we performed CMC simulations (reported in Section VII) for the lattice Hamiltonian in Eq. (1) to find out which of the sets of parameters identified above as candidate CSLs are indeed such (for 3-component spins) down to the lowest temperature.

Let us discuss now a simple and concrete example to demonstrate how to execute the above protocol, considering the classical spin ice spin liquid. This spin liquid is a non-Kramers spin case so  $a_{T_{1,p}} = 0$ , and the irreps  $\mathbf{m}_{T_{1,p}}$  and  $\mathbf{m}_{T_{1,i}}$  do not mix. Following the procedure, we have:

- *Step #0*: For this choice of  $a_X$  parameters, we have that  $\mathcal{E}_0 = a_{T_{1,i}}$  such that  $\mathcal{E}_0 < a_{A_2}, a_E, a_{T_{1,p}}, a_{T_2}$ .
- *Step #1*:  $a_{T_{1,i}}$  is minimal and the others  $a_X$  are not (ref. Table III) and, therefore, all other  $\mathbf{m}_Y = 0$ . However, despite a set of fields being frozen, their associated spin pattern constrains the fluctuating field  $\mathbf{m}_{T_{1,i}}$ . In the present case, the only other frozen “constraining field” acting onto the fluctuating  $\mathbf{m}_{T_{1,i}}$  field is  $m_{A_2} = 0$  (see Eq.(25)). We return to the role of this frozen constraining field in *Step #3* below.
- *Step #2*: As stated above, the only field able to thermally fluctuate in the present case is  $\mathbf{m}_{T_{1,i}}$ .
- *Step #3*: According to Eq. (25), the field  $\mathbf{m}_{T_{1,i}}$  is further constrained by  $m_{A_2} = 0 \implies \nabla \cdot \mathbf{m}_{T_{1,i}} = 0$ . This is exactly the Maxwell’s Gauss’s law, with the charge-free condition imposed for the ground state configurations,
- *Step #4*: Lastly, the band structure for this model yields two low-energy flat bands reflecting the extensive degeneracy associated with this spin liquid. This is because the emergent electric field has three DOFs, and there is one constraint, namely  $m_{A_2} = 0$ .

## IV. CSLS FOR NON-KRAMERS SPINS

### A. Identification of CSLS for non-Kramers spins

We are now ready to employ the methodology developed in Sec. III to systematically scan over the whole parameter space  $\{J_{zz}, J_{\pm}, J_{\pm\pm}, J_{z\pm}\}$  of the nearest-neighbor Hamiltonian in Eq. (1) without the single-ion

anisotropy term in Eq. (3). First, in this section, we report all the CSLs we identified in the case of non-Kramers spin models. As discussed above, in this case  $a_{T_{1,p}}$  vanishes, so  $\mathbf{m}_{T_{1,p}}$  and  $\mathbf{m}_{T_{1,i}}$  are the correct irreps in the diagonalized form of the single-tetrahedron Hamiltonian. Following Step #3, we then use Eqs. (25-29) to derive the Gauss’s laws. Following our procedure, we identified a total of five different types of CSLs, which are discussed in detail below. The non-Kramers spin liquids are listed in Table I as CSL 1-5, and their location in the phase diagram is reported in Fig. 2.

**CSL 1. Single R1U1 (Spin ice):** The first case is the well-known spin ice (although in our work the spins are 3-component spins instead of hard (1-component) Ising spins, it does not affect the properties of the ground states). In this case, the coefficient  $a_{T_{1,i}}$  is minimal, and all the other coefficients are greater than  $a_{T_{1,i}}$ . The effective physics of this spin liquid was already analyzed as the simplest example of the inter-tetrahedron coarse-graining rule at the end of Sec. III C, Eqs. (25).

As shown there, a Gauss’s law is obtained, given by

$$m_{A_2} = 0 \implies \nabla \cdot \mathbf{m}^{\text{ice}} \equiv \nabla \cdot \mathbf{E}^{\text{ice}} = 0, \quad (34)$$

which is equivalent to the Maxwell U(1) Gauss’s law. As well-known for this regime, the charge (in some literature referred to as magnetic monopole) is measured by  $m_{A_2} = S_1^z + S_2^z + S_3^z + S_4^z$ , and imposes the microscopic 2-in-2-out “ice-rule” for the ground states [18, 86].

**CSL 2. Double R1U1 (SL $_{\perp}$ ):** The second CSL that we consider in the phase diagram arises when  $a_{T_{1,p}}$  and  $a_{T_2}$  are minimal, and the other  $a_Y$ ’s are not. In this case, the vanishing field  $\mathbf{m}_E = 0$  imposes constraints on the  $\mathbf{m}_{T_{1,p}}$  and  $\mathbf{m}_{T_2}$  fluctuating fields. The constraints are given by Eq. (26). This can be written as two copies of a Maxwell U(1) Gauss’s law:

$$\mathbf{m}_E = 0 \implies \nabla \cdot \mathbf{E}^A = 0 \text{ and } \nabla \cdot \mathbf{E}^B = 0, \quad (35)$$

where

$$\mathbf{E}^A = (2m_{T_{1,p}}^x, -m_{T_{1,p}}^y - \sqrt{3}m_{T_2}^y, \sqrt{3}m_{T_2}^z - m_{T_{1,p}}^z), \quad (36)$$

$$\mathbf{E}^B = (2m_{T_2}^x, \sqrt{3}m_{T_{1,p}}^y - m_{T_2}^y, -\sqrt{3}m_{T_{1,p}}^z - m_{T_2}^z). \quad (37)$$

This CSL was identified and studied in Ref. [60]. It was found that the system remains in a spin liquid state down to a fairly low temperature and that the dipolar spin-spin correlations in that regime are indeed described by a double U(1) Gauss’s law. At very low temperatures, a hidden order quadrupolar develops in which the spins spontaneously select a particular axis in the local  $xy$ -plane along which they to co-align. Nevertheless, the spin correlations remain algebraic.

**CSL 3. Triple R1U1 (pHAF) :** In this case,  $a_{T_{1,p}}$ ,  $a_{T_{1,i}}$  and  $a_{T_2}$  are minimal, and the other ones are not. For these parameters, CSL 1 and CSL 2 become degenerate.

As a consequence, this CSL is described by an emergent spin ice  $\times$  Double U(1) field. This gives rise to three copies of Maxwell U(1) Gauss's laws which can be written compactly as

$$\partial_i E_{ij}^{\text{pHAF}} = 0, \quad (38)$$

where  $\mathbf{E}^{\text{pHAF}}$  is a  $3 \times 3$  matrix,

$$\mathbf{E}^{\text{pHAF}} = [(\mathbf{E}^{\text{ice}})^T, (\mathbf{E}^{\text{A}})^T, (\mathbf{E}^{\text{B}})^T]. \quad (39)$$

We note that this CSL 3 state corresponds to the so-called pseudo-Heisenberg AFM point in parameter space [60]. The above description of this CSL is consistent with the understanding that it is equivalent to the HAFM model [58, 59], but now for spins in their local basis, hosting three copies of U(1) Maxwell Gauss's law, one for each component of  $\mathbf{S}$ .

#### CSL 4. R1U1-R2U1 ( $\mathbf{R}_1\text{-}\mathbf{R}_2^{\text{T}_1}$ ):

In this case,  $a_{\mathbf{E}}$ ,  $a_{\text{T}_{1,p}}$  and  $a_{\text{T}_{1,i}}$  are minimal, and the other  $a_{\mathbf{V}}$ 's are not. The constraints give two co-existing Gauss's laws,

$$m_{\mathbf{A}_2} = 0 \implies \nabla \cdot \mathbf{E}^{\text{ice}} = 0, \quad (40)$$

$$\mathbf{m}_{\text{T}_2} = 0 \implies$$

$$\sqrt{3}\nabla \times \mathbf{m}_{\text{T}_{1,p}} + \begin{pmatrix} 2\partial_x m_{\mathbf{E}}^2 \\ -\sqrt{3}\partial_y m_{\mathbf{E}}^1 - \partial_y m_{\mathbf{E}}^2 \\ \sqrt{3}\partial_z m_{\mathbf{E}}^1 - \partial_z m_{\mathbf{E}}^2 \end{pmatrix} = 0. \quad (41)$$

The first equation is the Maxwell Gauss's law for spin ice, whereas the second equation can be rewritten in a compact form as a rank-2 "electric field"  $\mathbf{E}_{ij}^{\text{T}_1+\mathbf{E}}$  with off-diagonal anti-symmetric and diagonal traceless components, defined as

$$\mathbf{E}^{\text{T}_1+\mathbf{E}} = \begin{pmatrix} 2m_{\mathbf{E}}^2 & \sqrt{3}m_{\text{T}_{1,p}}^z & -\sqrt{3}m_{\text{T}_{1,p}}^y \\ -\sqrt{3}m_{\text{T}_{1,p}}^z & -\sqrt{3}m_{\mathbf{E}}^1 - m_{\mathbf{E}}^2 & \sqrt{3}m_{\text{T}_{1,p}}^x \\ \sqrt{3}m_{\text{T}_{1,p}}^y & -\sqrt{3}m_{\text{T}_{1,p}}^x & -\sqrt{3}m_{\mathbf{E}}^1 - m_{\mathbf{E}}^2 \end{pmatrix}. \quad (42)$$

Using the rank-2 tensor, the following vector charge Gauss's law, i.e. a higher-rank Gauss's law, is obtained

$$\partial_i E_{ij}^{\text{T}_1+\mathbf{E}} = 0. \quad (43)$$

We note that the higher-rank Gauss's law resembles that of rank-2 U(1) gauge theory, but it is not the symmetric tensor version [87, 88]. In particular, this CSL 4 harbours *infinitely many* multipole-charge conservation laws. Defining  $\rho_j = \partial_i E_{ij}^{\text{T}_1+\mathbf{E}}$ , we obtain the following conserved quantities:

$$f(x+y+z)(\rho_1 + \rho_2 + \rho_3), \quad (44)$$

$$g(x-y-z)(\rho_1 - \rho_2 - \rho_3), \quad (45)$$

$$k(-x+y-z)(-\rho_1 + \rho_2 - \rho_3), \quad (46)$$

$$l(-x-y+z)(-\rho_1 - \rho_2 + \rho_3), \quad (47)$$

where  $f(w)$ ,  $g(w)$ ,  $k(w)$ ,  $l(w)$  are arbitrary polynomials of the argument  $w$ . As an example, if we define  $w = x+y+z$ , the dipole  $w(\rho_1 + \rho_2 + \rho_3)$ , quadrupole  $w^2(\rho_1 + \rho_2 + \rho_3)$ , etc., are all conserved along the [111] direction. Such multipole-charge conservation laws apply to all the [111] directions.

This CSL, and also the next one discussed just below, CSL 5, was very recently identified and studied in Ref. [62]. This CSL is interesting in that it displays two distinct spin-liquidity regimes as a function of temperature: at intermediate temperature, the energy-degenerate  $\mathbf{E}$  and both  $\text{T}_1$  irreps are thermally populated, resulting in the so-called rank-1–rank-2 ( $\text{R}_1\text{-}\text{R}_2$ ) spin liquid in which two-fold and four-fold pinch points in the spin correlation functions are observed. At low temperatures, the model presents a thermal depopulation of the  $\mathbf{E}$  and the  $\text{T}_{1,p}$  associated with an entropic selection of the  $\text{T}_{1,i}$ , leading to a spin-ice-like CSL. The phenomenology observed in this model is reminiscent of a liquid-to-liquid transition in some molecular liquids such as phosphorous [89], sulfur [90], and silicon [91]. We note that the additional  $\text{T}_1$  label for the CSL 4 indicates that the rank-2 tensor has a  $\text{T}_1$  field dependence whereas the CSL 5 has a dependence of the  $\text{T}_2$  field as is further discussed below.

**CSL 5. R1U1-R2U1 ( $\mathbf{R}_1\text{-}\mathbf{R}_2^{\text{T}_2}$ )** In this case,  $a_{\mathbf{E}}$ ,  $a_{\text{T}_2}$  and  $a_{\text{T}_{1,i}}$  are minimal, and the other ones not. It is the same spin liquid as the above CSL 4 via a duality which corresponds to local  $\pi/2$  rotation defined as

$$\begin{aligned} (S^x, S^y) &\rightarrow (-S^y, S^x), \\ J_{\pm\pm} &\rightarrow -J_{\pm\pm}, \end{aligned} \quad (48)$$

or, alternatively,  $S_j^\pm \rightarrow \pm i S_j^\pm$ . In terms of the irreps, this duality implies  $m_{\mathbf{E}}^1 \leftrightarrow m_{\mathbf{E}}^2$  and  $\mathbf{m}_{\text{T}_2} \leftrightarrow \mathbf{m}_{\text{T}_{1,p}}$ . Implementing these dualities on the rank-2 tensor  $\mathbf{E}^{\text{T}_1+\mathbf{E}}$ , we obtain the dual rank-2 tensor  $\mathbf{E}^{\text{T}_2+\mathbf{E}}$ . Altogether, the Gauss's law describing this CSL 5 are

$$\begin{aligned} m_{\mathbf{A}_2} = 0 &\implies \nabla \cdot \mathbf{E}^{\text{ice}} = 0, \\ \mathbf{m}_{\text{T}_{1,p}} = 0 &\implies \partial_i E_{ij}^{\text{T}_2+\mathbf{E}} = 0, \end{aligned} \quad (49)$$

where  $\mathbf{E}^{\text{T}_2+\mathbf{E}}$  is defined similarly as  $\mathbf{E}^{\text{T}_1+\mathbf{E}}$ , but now, by making replacement  $\mathbf{m}_{\text{T}_{1,p}} \rightarrow \mathbf{m}_{\text{T}_2}$  and  $(m_{\mathbf{E}}^1, m_{\mathbf{E}}^2) \rightarrow (-m_{\mathbf{E}}^2, m_{\mathbf{E}}^1)$ . Thanks to the duality (48), the thermodynamical properties of this CSL 5 are identical to those of the CSL 4. However, the spin correlations themselves are different [62].

## B. Summary of the non-Kramers Hamiltonian

To summarize, in total, the non-Kramers spin model hosts five CSLs, listed in Table I. In the phase diagram of  $J_\pm - J_{\pm\pm} - J_{zz}$  illustrated in Fig. 2, only the spin ice (CSL 1) exists as a phase occupying a 3D volume;

all other CSLs sit on phase transition planes/lines separating long-range ordered phases. The spin ice phase takes the shape of an infinitely large, three-edged pyramid. The double U(1) CSL (CSL 2) occupies a plane attached to an edge of the pyramid. The CSLs 3, 4, 5 are located on the three edges of the pyramid defined by the spin ice phase, a feature further manifested by the fact that their respective Gauss's laws incorporate the Maxwell U(1) Gauss's law of spin ice.

Various interesting points on the phase diagram have been previously studied in the literature. Obviously, the most intensively studied one is spin ice. Beside it, the CSL 4 with its triple U(1) has also been *de facto* investigated in Ref. [60] as the pseudo-Heisenberg point and the double U(1) was studied in Ref. [60]. The  $R_1$ - $R_2^{\top 1}$  CSL 4 was very recently studied in Ref. [62]. There, the Hamiltonian of that model was coined the name dipolar-quadrupolar-quadrupolar (DQQ) model because it is realized at the triple point where two long-range ordered quadrupolar phases meet the disordered spin ice (dipolar) phase, discussed Refs. [32, 78]. The CSL 5 ( $R_1$ - $R_2^{\top 2}$ ) is realized at the dual point of the DQQ model, referred to as DQQ\* in Ref. [62], so these the CLS4 and CLS 5 exhibit identical thermodynamics.

We note that, although there are also three triple-phase-boundary points for the case where  $J_{zz} < 0$  (See Fig 2), which have three degenerate  $a_X$ 's, all of these exhibit a finite-temperature phase transition into an ordered state as found from CMC simulations. We refer the reader to Sec VIII for more details on these other specific models.

## V. CSLS FOR KRAMERS SPINS

### A. Identification of CSLs for Kramers spins

In this section, we discuss the case of the spin model for Kramers ions. In terms of the bilinear Hamiltonian in Eq. (1), Kramers spins allow for nonzero  $J_{z\pm}$  interaction. When rewriting the Hamiltonian in terms of the irreps as discussed in Sec. III A, an additional term as the coupling between the two  $T_1$  irreps  $\mathbf{m}_{T_{1,p}}$  and  $\mathbf{m}_{T_{1,i}}$  is now permitted in Eq. (5). Again, this originates from the fact that both  $S_i^z$  and  $S_i^{\pm}$  are time-odd, transforming as real spin-1/2 operators, and are coupled in Eq. (1). As previously discussed, the interaction between  $\mathbf{m}_{T_{1,p}}$  and  $\mathbf{m}_{T_{1,i}}$  via  $a_{T_{1,ip}}$  in Eq. (5), can be eliminated by a change of basis within the  $T_{1,i}$  and  $T_{1,p}$  sector, giving a new basis defined by the fields  $\mathbf{m}_{T_{1,+}}$  and  $\mathbf{m}_{T_{1,-}}$  which diagonalize the Hamiltonian  $H_t$ . The inter-tetrahedra constraints are then modified to be expressed in terms of these new  $\mathbf{m}_{T_{1,\pm}}$  fields. This is discussed in detail from Eq. (6) to Eq. (13). We now proceed to discuss the CSLs that arise when  $J_{z\pm}$ , or equivalently  $a_{T_{1,ip}}$ , is non-zero. As done above for the non-Kramers case, we apply the procedure discussed in Sec. III D with the inter-tetrahedron constraints of Eqs. (20-24) to systematically search for the

CSLs that Kramers ions can exhibit on the pyrochlore lattice. For the Kramers Hamiltonian, we have found in total four different types of CSLs, which are discussed in detail below. These CSLs are listed in Table I as CSL 6-9, and their phase diagram is shown in Fig. 3. There are actually two phase diagrams for  $J_{z\pm} > 0$  and  $J_{z\pm} < 0$  respectively, but the geometry of the two phase diagrams are identical as a consequence of an exact duality of the Kramers Hamiltonian associated to a change of sign in the  $J_{z\pm}$  coupling [16] which we discuss in further detail below.

### CSL 6. Scalar-vector-charge (SV) R2U1 CSL:

This CSL is stabilized when the parameters  $a_E$ ,  $a_{T_2}$ , and  $a_{T_{1,-}}$  are simultaneously minimal, when

$$\begin{aligned} J_{z\pm} &> 0, \\ J_{zz} &> -\frac{1}{\sqrt{2}}J_{z\pm}, \\ J_{\pm} &= \frac{1}{12} \left( J_{zz} + \sqrt{J_{zz}^2 + 24J_{z\pm}^2} \right), \\ J_{\pm\pm} &= \frac{1}{6} \left( J_{zz} + \sqrt{J_{zz}^2 + 24J_{z\pm}^2} \right). \end{aligned} \quad (50)$$

On the 3D phase diagram of fixed  $J_{z\pm}$ , these equations parametrize a line. The effective Gauss's law for this CSL has a scalar charge and a vector charge defined for its rank-2, traceless electric field,

$$m_{A_2} = 0 \implies |\epsilon^{ijk}| \partial_i E_{jk}^{SV} = 0, \quad (51)$$

$$\mathbf{m}_{T_{1,+}} = 0 \implies \partial_i E_{ij}^{SV} = 0, \quad (52)$$

where

$$\begin{aligned} \mathbf{E}^{SV} &= \begin{pmatrix} 2m_E^1 & \sqrt{3}m_{T_2}^z & -\sqrt{3}m_{T_2}^y \\ -\sqrt{3}m_{T_2}^z & -m_E^1 + \sqrt{3}m_E^2 & \sqrt{3}m_{T_2}^x \\ \sqrt{3}m_{T_2}^y & -\sqrt{3}m_{T_2}^x & -m_E^1 - \sqrt{3}m_E^2 \end{pmatrix} \\ &- 3 \sin \phi \begin{pmatrix} 0 & m_{T_{1,-}}^z & m_{T_{1,-}}^y \\ m_{T_{1,-}}^z & 0 & m_{T_{1,-}}^x \\ m_{T_{1,-}}^y & m_{T_{1,-}}^x & 0 \end{pmatrix}. \end{aligned} \quad (53)$$

Here,  $|\epsilon^{ijk}|$  is the absolute value of the Levi-Civita symbol. The Gauss's law explicitly breaks the continuous rotational symmetry, and exhibits both pinch-line and four-fold pinch points.

Defining  $\rho_0 = |\epsilon^{ijk}| \partial_i E_{jk}^{SV}$  and  $\rho_i = \partial_i E_{ij}^{SV}$ , we have the following infinitely many conservation laws:

$$f(x+y+z)(-\rho_0 + \rho_1 + \rho_2 + \rho_3), \quad (54)$$

$$g(x-y-z)(-\rho_0 + \rho_1 - \rho_2 - \rho_3), \quad (55)$$

$$k(-x+y-z)(-\rho_0 - \rho_1 + \rho_2 - \rho_3), \quad (56)$$

$$l(-x-y+z)(-\rho_0 - \rho_1 - \rho_2 + \rho_3). \quad (57)$$

As before,  $f(w)$ ,  $g(w)$ ,  $k(w)$ ,  $l(w)$  are arbitrary polynomials of  $w$ . We note that, although a similar gauge field as

that in Eq. (53) describing the low-temperature physics of the pinch-line spin liquid was identified [61], the precise details of the Gauss's laws, the conserved quantities, and the gauge charges associated with it were not discussed.

**CSL 7. SV R2U1\* (Pinch-line spin liquid):**

This CSL has the same degeneracy of minimal parameters as CSL 6:  $a_E$ ,  $a_{T_2}$ , and  $a_{T_{1,-}}$  which, in terms of spin exchange parameters, amount to the conditions

$$\begin{aligned} J_{z\pm} < 0, \quad J_{zz} > \frac{1}{\sqrt{2}}J_{z\pm}, \\ J_{\pm} &= \frac{1}{12} \left( J_{zz} + \sqrt{J_{zz}^2 + 24J_{z\pm}^2} \right), \\ J_{\pm\pm} &= \frac{1}{6} \left( J_{zz} + \sqrt{J_{zz}^2 + 24J_{z\pm}^2} \right). \end{aligned} \quad (58)$$

The corresponding emergent Gauss's laws have the same functional form as those of CSL 6. The low-temperature physics of both spin liquids are described by a rank-2 gauge field constraint by the Gauss's laws in Eq. (51) and Eq. (52). However, the precise definition of the  $m_{T_{1,-}}$  and therefore the gauge fields themselves are distinct. The CSLs 6 and 7 should therefore be considered as different. First, the microscopic Hamiltonian parameters defining the two CSLs are different. Second, on the phase diagram, the two CSLs do not directly connect to each other as they are separated by the limit of  $J_{z\pm} = 0$ , which corresponds to the distinct CSL 4. Nonetheless, CSL 6 and 7 are related by the duality [16, 54]

$$\begin{aligned} J_{z\pm} &\rightarrow -J_{z\pm}, \\ (S^x, S^y, S^z) &\rightarrow (-S^x, -S^y, S^z). \end{aligned} \quad (59)$$

More generally, this duality implies that the phase diagram boundaries between magnetic orders are identical after reversing the sign of  $J_{z\pm}$ , but the magnetic orders themselves are not identical on the two sides. This duality and the one of Eq. (48) are two different dualities for two different models. The later one applies for the non-Kramers Hamiltonian and is not (on its own) a duality of the Kramers Hamiltonian. The former one for  $J_{z\pm}$  in Eq. (59) only applies to the Kramers Hamiltonian while in the non-Kramers case, the consequential transformation on the  $xy$  components of the pseudospins in Eq. (48) amounts to a trivial reflection symmetry. This CSL 7 was studied in Ref. [61]. Here, our observation of an infinite number of conserved charges, the duality of Eq. (59), and also the overall structure of the phase diagram complement that previous study [61]. We provide in Section VII below numerical evidence for the persistence of the spin liquid behavior for this phase for distinct values of  $J_{z\pm}$  down to the lowest temperatures.

**CSL 8. Triple R1U1 (HAFM):** The second to last CSL that we identify is the well-known Heisenberg antiferromagnet (HAFM) [58, 59, 92, 93]. This CSL corresponds to the point where the CSL 6 meets the AIAO

phase with the  $a_E$ ,  $a_{T_2}$ ,  $a_{T_{1,-}}$ , and  $a_{A_2}$  interaction parameters all being minimal. The spin-spin interaction parameters for this CSL are parametrized as

$$\begin{aligned} J_{z\pm} > 0, \quad J_{zz} &= -\frac{1}{\sqrt{2}}|J_{z\pm}|, \\ J_{\pm} &= \frac{1}{2\sqrt{2}}|J_{z\pm}|, \quad J_{\pm\pm} = \frac{1}{\sqrt{2}}|J_{z\pm}|. \end{aligned} \quad (60)$$

This point corresponds to the isotropic  $O(3)$  Heisenberg antiferromagnetic model in the global spin basis. The Gauss's law for this CSL are three copies of  $U(1)$ , written in a compact form as

$$m_{T_{1,+}} = 0 \implies \partial_i E_{ij}^{\text{HAF}} = 0, \quad (61)$$

where

$$E_{ij}^{\text{HAF}} = E_{ij}^{\text{SV}} - 2\delta_{ij}(\tan\phi)m_{A_2}. \quad (62)$$

We see here that the scalar  $m_{A_2}$  field adds exactly to the trace component to the otherwise traceless  $E_{ij}^{\text{SV}}$  rank-2 field such that  $E_{ij}^{\text{HAF}}$  acquires the full nine degrees-of-freedom associated to a three-by-three matrix. These DOFs correspond to the nine components of the degenerate  $m_{\chi}$  fields, whose trace is the  $m_{A_2}$  field, two diagonal, traceless elements are the  $m_E$  field, three off-diagonal, antisymmetric elements are the  $m_{T_2}$  field, and three off-diagonal, symmetric elements are the  $m_{T_{1,-}}$  field. Altogether, these nine degrees of freedom and the three Gauss's laws in Eq. (61) result in six degenerate low-energy flat bands describing the ground state manifold of this CSL [58].

**CSL 9. Triple R1U1 (HAFM\*):** The last CSL for the Kramers Hamiltonian that we identify is dual to the HAFM CSL 8, with  $J_{z\pm} < 0$  and parametrized as

$$\begin{aligned} J_{z\pm} < 0, \quad J_{zz} &= -\frac{1}{\sqrt{2}}|J_{z\pm}|, \\ J_{\pm} &= \frac{1}{2\sqrt{2}}|J_{z\pm}|, \quad J_{\pm\pm} = \frac{1}{\sqrt{2}}|J_{z\pm}|. \end{aligned} \quad (63)$$

The emergent Gauss's law of this CSL is identical to that of the HAFM CSL. Nevertheless, this CSL should be considered a different CSL, as the dual of HAFM via Eq. (59). Indeed, the Hamiltonian for this CSL in the global spin basis is different from the HAFM as we further discuss in Appendix A.

## B. Summary of the Kramers Hamiltonians

To summarize, the Hamiltonian for Kramers ions hosts a total of four CSLs as listed in Table I. In this case, the CSLs 6 and 7 are dual to each other, and so are CSLs 8 and 9, with the two dual partners in each pair yielding identical thermodynamic properties (see Section VII). Similar to the non-Kramers, the CSLs identified in the

Kramers Hamiltonian separate distinct long-range ordered phases where the CSL 8 (9) corresponds to the tip of a pyramid corresponding to an  $A_2$  phase where the  $E$ , the  $T_{1,-}$  and the  $T_2$  long-range ordered phases meet. On the other hand, the CSL 6 (7) corresponds to a departure of these maximally-degenerated points by gaping out the  $A_2$  phase, as shown in Fig. 3. In the next section we discuss how these CSLs are connected to each other and what the consequences for their respective gauge theory are.

The above classical spin liquids that we identified constitute the full list of classical spin liquids that can be realized in Kramers and non-Kramers pyrochlores with only nearest-neighbor bilinear interactions. We reiterate that the present section and Section IV only discuss the non-Kramers and Kramers nearest-neighbor bilinear spin Hamiltonians, respectively, but do not consider the special case of dipolar-octupolar Kramers systems as this particular spin model has been exhaustively discussed in a previous work [36, 38]. In the following section, we discuss how and in what circumstances these spin liquids evolve from one to the other as the  $J_{uv}$  exchange parameters are modified.

## VI. CONNECTIVITY OF THE CLASSICAL SPIN LIQUIDS AND EVOLUTION OF THEIR EFFECTIVE GAUGE THEORIES

In this section, we discuss the overall landscape of the CSLs that the anisotropic bilinear spin Hamiltonian of Eq. (1) on the pyrochlore lattice harbors. A hierarchy structure exists for these CSLs: generally, the CSLs with more degrees-of-freedom (DOFs) of low-energy fluctuations (more components in the emergent electric field and fewer constraints) require more  $a_X$ 's [see Eq. (5)] to be degenerate. As a consequence, such CSLs live in a subspace of lower dimension in the parameter space. Furthermore, the CSLs with more DOFs are often connected to the other CSLs with more constrained Gauss's laws – the latter typically arising from lifting up some of the  $a_X$ 's out of the lowest value degeneracy.

For example, the CSL 3 (pHAF) is a CSL with 6 DOFs of low energy fluctuation. These correspond to the remaining 6 DOFs resulting from the three 3-dimensional irreps being degenerate constrained by the three Gauss's laws. In particular, by lifting the degeneracy of one of the irrep modes,

$$(a_{T_{1,i}}, a_{T_{1,p}}, a_{T_2}) \rightarrow (a_{T_{1,p}}, a_{T_2}),$$

we obtain the CSL 2 (Double U(1)). On the other hand, by lifting the degeneracy  $(a_{T_{1,i}}, a_{T_{1,p}}, a_{T_2}) \rightarrow a_{T_{1,i}}$ , we obtain the CSL 1 (i.e. spin ice).

Another example is the transformation from CSL 8 to CSL 6 (and equivalently CSL 9 to CSL 7), which is effectuated by the following degeneracy lifting

$$(a_{A_2}, a_E, a_{T_{1,-}}, a_{T_2}) \rightarrow (a_E, a_{T_{1,-}}, a_{T_2}).$$

In these transitions, the resulting Gauss's laws are obtained from the old ones by reducing the components of the electric field and/or adding new constraints.

Let us now discuss the transitions between different CSLs in more detail. First, let us elaborate on an important fact about the CSLs 6 and 7. As discussed in Section V, the parameter space identified in Eq. (50) for each one of these CSLs correspond to a 2D surface, with no symmetry-breaking phase transition detected in Monte Carlo simulations down to the lowest temperatures, as we discuss in Sec. VII. At low temperatures, an effective Gauss's laws are imposed on an emergent rank-2 field constructed in terms of the  $E$ ,  $T_2$ , and  $T_{1,-}$  irreps. This is the case for any point in the parameter space characterizing these two CSLs. However, it is crucial to realize that, although the form of the effective gauge theory remains the same, the precise constituents of the rank-2 field in terms of spins differ. Such variation is captured by the dependence of the rank-2 tensor on the parameters  $\{v_{i\pm}, v_{p\pm}\}$  that define the  $T_{1,-}$  irrep [Eqs. (6,7)]. Indeed, by tuning the constituents of the rank-2 fields we are also effectively tuning the definition of the charge in these spin liquids. Consequently, one may understand the 2D spin liquid manifolds as a continuous set of models whose low-energy emergent electric fields are smoothly evolving while fulfilling a Gauss's law constraint.

Having discussed how the effective gauge theories in the CSL 6 and CSL 7 smoothly evolve as the microscopic Hamiltonian parameters evolve while keeping the system in one of the CSLs, we now turn to consider how these CSLs are connected to each other. Figure 5 illustrates a phase diagram where the region of stability of multiple CSLs is shown. There we take  $J_{zz}$  and  $J_{z\pm}$  to be free parameters while  $(J_{\pm}, J_{\pm\pm})$  are implicitly fixed by Eq. (50) and Eq. (58). We first note that the two parameter spaces defining the CSL 6 and CSL 7 meet on the line defined by  $\{J_{zz}, J_{\pm}, J_{\pm\pm}, J_{z\pm}\} = \{J, J/6, J/3, 0\}$  with  $J > 0$ . This line, shown as the white dashed line in Fig. 5, corresponds to the CSL 5 [62], where the rank-2 fields break down into one rank-2 field and one rank-1 field, each fulfilling an independent Gauss's law. In particular, for the CSL 6, the gauge field  $\mathbf{E}^{SV}$  in Eq. (53) and the Gauss's laws in Eq. (51)-(52) decompose into the rank-1  $\mathbf{E}^{ice}$  and the rank-2  $\mathbf{E}^{T_1+E}$  electric fields constrained by the Gauss's laws in Eq. (49). Importantly, this is the limit of vanishing  $J_{z\pm}$  which characterizes non-Kramers ions discussed in Sec. IV <sup>4</sup>.

The other boundaries of the CSL 6 and 7 parameter spaces are located at  $J_{zz} = -\left|\frac{1}{\sqrt{2}}J_{z\pm}\right|$  with  $J_{z\pm}$  positive

<sup>4</sup> Here we note that the interaction parameters corresponding to the CSL 5 in Fig. 5 are such that the ratio  $J_{zz} : J_{\pm} : J_{\pm\pm} = 6 : 1 : 2$  is always fulfilled therefore identifying a 1D region as a function of  $J_{zz}$ . The evolution of these parameters can be obtained by simply taking the parametrization of the CSLs 6 and 7, Eqs. (50) and (58), while setting  $J_{z\pm} = 0$ .

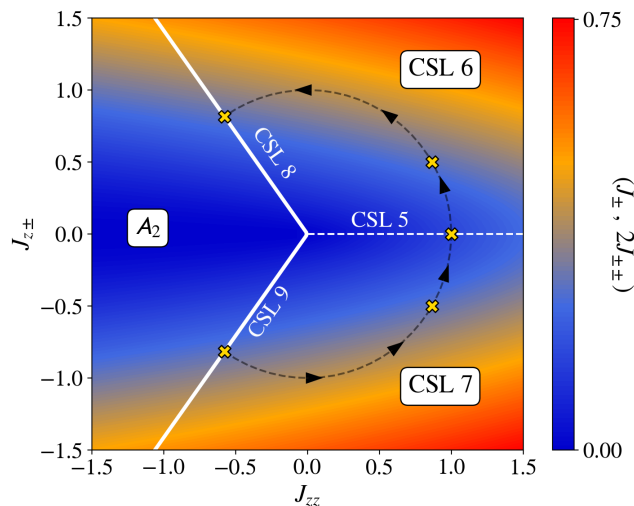


FIG. 5. Phase diagram illustrating the how the classical spin liquids (CSLs) transition into/connect with each other. The plot is on axis of  $J_{zz}$  and  $J_{z\pm}$ , and  $J_{\pm}$ ,  $J_{\pm\pm}$  take values based on Eqs. (50,58). The upper right wedge is CSL 6, and lower right edge is CSL 7. The solid white lines, corresponding to CSL 8 and CSL 9, set the boundary between the spin liquid regime and the symmetry-breaking  $A_2$  (AIAO) phase. The dashed white line separating CSL 6 and CSL 7 is the CSL 5. The reflection symmetry of the phase diagram along  $x$ -axis is the consequence of the duality of Eq. (59). Lastly, the black dashed line indicates a way of tuning between the different spin liquids where the yellow crosses represent models for which the structure factors are shown in Fig. 6.

for the CSL 6 while it is negative for the CSL 7. These boundaries correspond to the CSL 8 (for  $J_{z\pm} > 0$ ), and CSL 9 (for  $J_{z\pm} < 0$ ), respectively. These boundaries, marked by solid white lines in Fig. 5, separate the CSL 6 and 7 from the  $A_2$  (all-in/all-out, AIAO) magnetically ordered phase. As discussed at the beginning of this section, the CSLs 8 and 9, “viewed” as the boundary of CSLs 6 and 7 with the magnetically ordered  $A_2$  phase, have a higher degeneracy. The CSL 8 and 9 are thus CSLs with a higher number of low-energy-fluctuation DOFs [Eq. (61)], and contain all of the fluctuating DOFs of the CSLs 6 and 7 [Eq. (51)].

We have now discussed how the CSLs 6 and 7 have a smoothly varying definition of electric field subjected to the emergent Gauss’s laws, and how they are connected to other CSLs on the boundary within the parameter space that define them. From an experimental context, such a variation of the electric field can be exposed via the equal time polarized and unpolarized neutron structure factors which evolve as a function of the  $J_{z\pm}$  and  $J_{zz}$  coupling parameters. Figure 6 illustrates the spin structure factor, unpolarized and polarized (spin flipping (SF) channel and non-spin flipping (NSF) channel) neutron structure factor in the  $[hk0]$  plane for five different sets of parameters marked by yellow crosses in Fig. 5, which correspond to CSLs 9, 7, 5, 6, 8 in the respective

order. The data illustrated here was obtained using a large- $\mathcal{N}$  approximation which yields qualitatively similar results to those obtained with CMC simulations, except for the case with  $J_{z\pm} = 0$  in the  $T \rightarrow 0$  limit which displays disorder-by-disorder selection of a spin ice ground state [62]. In this figure, and heretofore, we consider an isotropic  $g$  tensor assuming that the fluctuations in all spin components are taken in equal footing [62, 94]. We refer the reader to Appendix C for the explicit definition of these correlation functions and for a short discussion regarding the choice of an isotropic  $g$  tensor used in these calculations. For the CSLs 5, 6 and 7, their effective gauge theories are characterized by an emergent Gauss’s law of a rank-2 electric field. The latter results in the presence of four-fold pinch points in the correlation functions, besides the familiar two-fold pinch points, see Fig. 6 where white circles (squares) in the unpolarized neutron structure factor (polarized NSF channel) indicate the location of two-fold (four-fold) pinch points. Although these anisotropic features are preserved by the structure factors, the overall intensity distribution significantly changes reflecting the evolving nature of the gauge fields and its functional dependence on the parametrization used in Fig. 5.

We note that the CSL 9 (HAFM\*) also exhibits four-fold pinch points in its neutron structure factor at the  $\Gamma$  point, although its Gauss’s law is not that associated to a higher-rank field. This four-fold pinch point is instead the consequence of the neutron-spin coupling form factor [95] being non-analytical at the  $\Gamma$  point – it is not caused by the emergent gauge structure of the model. We therefore conclude that, although the observation of four-fold pinch points is often a strong indication of an emergent higher-rank gauge theory, when observed at the  $\Gamma$  point, it is strictly neither a necessary nor a sufficient condition for the identification of such an underlying gauge theory<sup>5</sup>. This analysis therefore highlights the importance of studying the different accessible scattering channels to expose the anisotropic features associated with the realization of an emergent gauge theory, in addition to the development of an accompanying field theory analysis, as elaborated in Sec. III, to unequivocally identify a spin liquid phase and its underlying gauge theory.

As a final remark, we note that by combining the results summarized by the phase diagrams in Figs. 2, 3, and 5, we have established that *all* CSLs in Table. I are *continuously* connected without having to pass through any conventional symmetry-breaking phase in the  $\{J_{zz}, J_{\pm}, J_{\pm\pm}, J_{z\pm}\}$  parameter space. For example,

<sup>5</sup> We note that the CSL 5 exhibits a four-fold pinch point at (020) and symmetry-related points in its unpolarized neutron structure factors shown in third row of Fig. 6. These four-fold pinch points are produced by the combination of two overlapping two-fold pinch points, one coming from the rank-1 field (spin ice) and another from the rank-2 field (the  $\mathbf{E}^{T_2+E}$  field), and cannot be taken on its own as an indication of an emergent rank-2 gauge theory.

from Figs. 3 and 5, we see that the Kramers CSLs 6, 7, 8 and 9, and the non-Kramers CSL 5 connect to each other. In addition, Fig. 2 shows that all the other non-Kramers CSLs connect to the CSL 5. The overall structure, or shape, of the parameter space of CSLs resembles that of an octopus: the “main body” (i.e. the extended volume phase in parameter space) corresponds to the spin ice state, and various surfaces and lines define the other CSLs that extend out of the body.

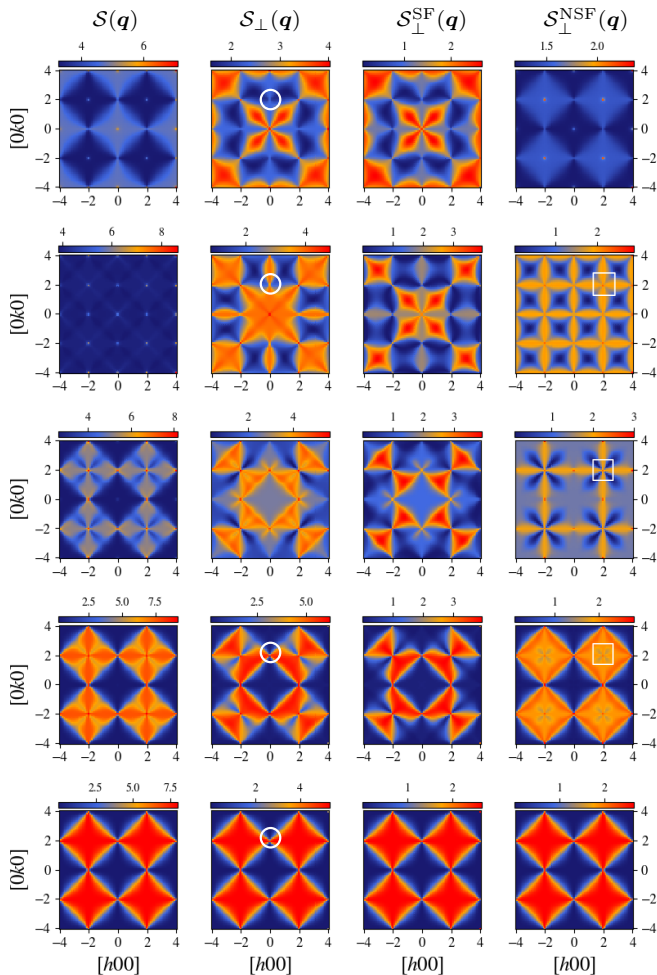


FIG. 6. Evolution of the spin structure factor (first column), neutron structure factor (second column), polarized neutron structure factor in the SF channel (third column), and polarized neutron structure factor in the NSF channel (fourth column) in the  $[hk0]$  plane, computed using the large- $\mathcal{N}$  approximation. In this figure, each row corresponds to a model parameterized by Eq. (50) labeled by the yellow crosses in Fig. 5 starting from the upmost row with the CSL 9 (HAFM\*) and ending in the bottom row with the CSL 8 (HAFM), as indicated by the black circling arrows in Fig. 5. The white circles (squares) indicate the location of a two-fold (four-fold) pinch point. Definitions of each structure factor are given in Appendix C.

So far, we have presented an analysis of the gauge theories describing the low temperature behavior of all pos-

sible CSLs realized by the generic anisotropic nearest-neighbor bilinear Hamiltonian on the pyrochlore lattice. Moreover, we have identified the features in reciprocal space correlation functions that can allow to an identification of those CSLs. In the next section, we present a classical Monte Carlo (CMC) numerical study of the heretofore unexplored new CSLs identified in this work. In doing so, we compare the CMC results on these models with the predictions obtained from their respective gauge theory and the large- $\mathcal{N}$  approximation.

## VII. BEYOND LARGE- $\mathcal{N}$ : THERMODYNAMICS AND STRUCTURE FACTORS FROM CLASSICAL MONTE CARLO

In this section, we discuss classical Monte Carlo (CMC) simulations of the interesting CSLs. In fact, we have performed CMC simulations for all the potential new CSLs identified by the field theory to confirm that they do not exhibit magnetic order down to the lowest temperatures since the field theory does not fully capture the  $\mathbf{S}^2 = 1$  constraint of every spin. Such CSLs are those listed in Table I. The other CSL candidates, corresponding to models located at the phase boundaries between the  $A_2$  and two additional  $\mathbf{q} = 0$  magnetic orders, actually order at low temperatures, and are discussed in the Sec VIII.

In the following, we present the thermodynamics of CSLs 6, 7, and 9 obtained via CMC simulations. The CSL 7 has already been discussed in Ref. [61], but its dual CSL 6, obtained via Eq. (59), has not been discussed in literature. Although the two CSLs have the same effective theory, their structure factors display drastically different patterns. The same applies to CSL 9, which is dual to HAFM via the same equation (59). We show the specific heat and spin structure factor for three CSL points marked in Fig. 5 by golden crosses, and whose structure factors are displayed in Fig. 6 in the first (uppermost row), second, and fourth rows.

For our simulations, we considered a system of  $4L^3$  spins with  $L = 10$  and update the system via a Gaussian spin-flip update [96], and an over-relaxation update [97, 98], in addition to averaging up to 10 independent CMC runs. We performed  $8 \times 10^4$  thermalization sweeps and  $2 \times 10^5$  measurement sweeps where we measured the energy, specific heat, and spin structure factors of the systems considered.

Figures 7 and 8 show the eigenvalue (bands) of the interaction matrix in momentum space, the specific heat, and the spin structure factors obtained for the parameters marked by the yellow crosses for the CSL 6 and CSL 7 in Fig. 5, respectively. As expected, and in agreement with the field analysis performed above, the band structure of the corresponding interaction matrices for these systems host four low-energy flat bands in their spectra (resulting from the 8 degrees of freedom and 4 constraints given by the Gauss’s laws), see panel Figs. 7(a) and 8(a). The resemblance between the band structure



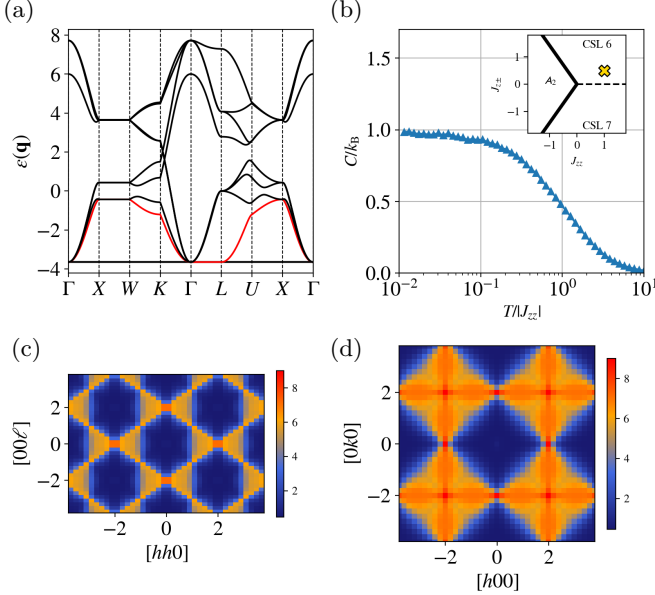


FIG. 7. (a) Diagonalized interaction matrix [Eq. (5)] band in reciprocal space for CSL 6, using parameters  $\{J_{zz}, J_{z\pm}\} = \{1, 0.5\}$  [Eq. (50)] where the first dispersive band is colored in red. There are four flat bands at the bottom in the spectrum. (b) Specific heat of the model, showing no sharp phase transitions from the paramagnetic phase down to the lowest temperature. The inset in this figure shows the precise location of the model in the phase diagram shown in Fig. 5. (c,d) spin structure factors in the  $[hh\ell]$  and  $[hk0]$  planes of the model.

of these two models is a consequence of the duality of the Hamiltonian [Eq. (1)] via Eq. (59). Neither models show a sign of symmetry-breaking transition as indicated by the smooth evolution of the specific heat of both systems, see Fig. 7(b) and Fig. 8(b). The spin structure factors for both systems are shown in Fig. 7(c)-(d) and Fig. 8(c)-(d) for the  $[hh\ell]$  and  $[hk0]$  reciprocal space planes, respectively, showing excellent agreement with the predictions obtained via large- $\mathcal{N}$  in Fig. 6.

In addition to the multifold pinch point anisotropies, we note that a distinctive feature in the correlation functions of CSL 7 is the observation of pinch lines, which can be observed in Fig. 8(c) along the  $[111]$  and symmetry-related directions. In a large- $\mathcal{N}$  theory, these features are produced by a dispersive band which, along the  $[111]$  direction, becomes degenerate with the low-energy flat bands, see the first dispersive band marked in red in Fig. 7(a) and Fig. 8(a). Reference [61] noted that for the CSL 7 singular features (i.e. pinch points) in the reciprocal space correlation function are observed along the location of the pinch line in reciprocal space. In particular, four-fold pinch points can be observed at the intersection of multiple pinch lines. Given that the CSL 6 is dual to the CSL 7, pinch lines should be observed in the structure factor of CSL 6. Although it is not immedi-

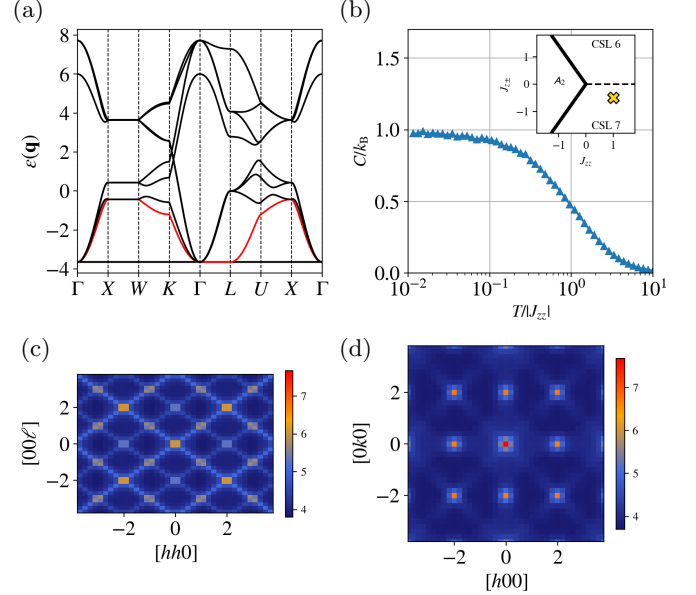


FIG. 8. (a) Diagonalized interaction matrix [Eq. (5)] band in reciprocal space for CSL 7, using parameters  $\{J_{zz}, J_{z\pm}\} = \{1, -0.5\}$  [Eq. (58)] where the first dispersive band is colored in red. The spectrum is identical to Fig. 7 due to the duality of Eq. (59) between the two models. (b) Specific heat of the model, showing no sharp phase transitions from the paramagnetic phase down to the lowest temperature. The inset in this figure shows the precise location of the model in the phase diagram shown in Fig. 5. (c,d) spin structure factors in the  $[hh\ell]$  and  $[hk0]$  planes of the model. Although CSL 6 and CSL 7 are dual to each other, their spin structure factor is different.

ately clear from the structure factors in Fig. 7(c) and (d) where these features appear, we may track the location of the pinch lines by studying the spinstructure factor in the vicinity of a four-fold pinch point. Figure 9 illustrates the spin structure factor for the CSL 6 in the  $[hk\Delta\ell]$  plane for increasing values of  $\Delta\ell$  obtained via CMC and the large- $\mathcal{N}$  method (see Appendix D) where the intersection of the black dashed lines tracks the location of one of the four pinch lines intersecting at the  $[220]$  point. We note that, in both CMC and large- $\mathcal{N}$ , as  $\Delta\ell$  is increased, the four-fold pinch point (in the  $[hk\Delta\ell]$  plane with  $\Delta\ell = 0$ ) splits into four two-fold pinch points. The location of the two-fold pinch points with respect to the four-fold pinch point is consistent with a  $\mathbf{q}$  vector  $\Delta\ell \times [111]$  and symmetry-related directions, corresponding to  $\mathbf{q}$  vectors where pinch lines are observed.

Lastly, we present in Fig. 10 the CMC results for CSL 9 corresponding to the dual HAFM model (HAFM\*). This model presents the same functional form of the energy bands as the regular HAFM where the six low-energy bands of the interaction matrix are flat; see Fig. 10(a). Furthermore, and as found for the HAFM [92], the specific heat of this model presents no sign of symmetry-

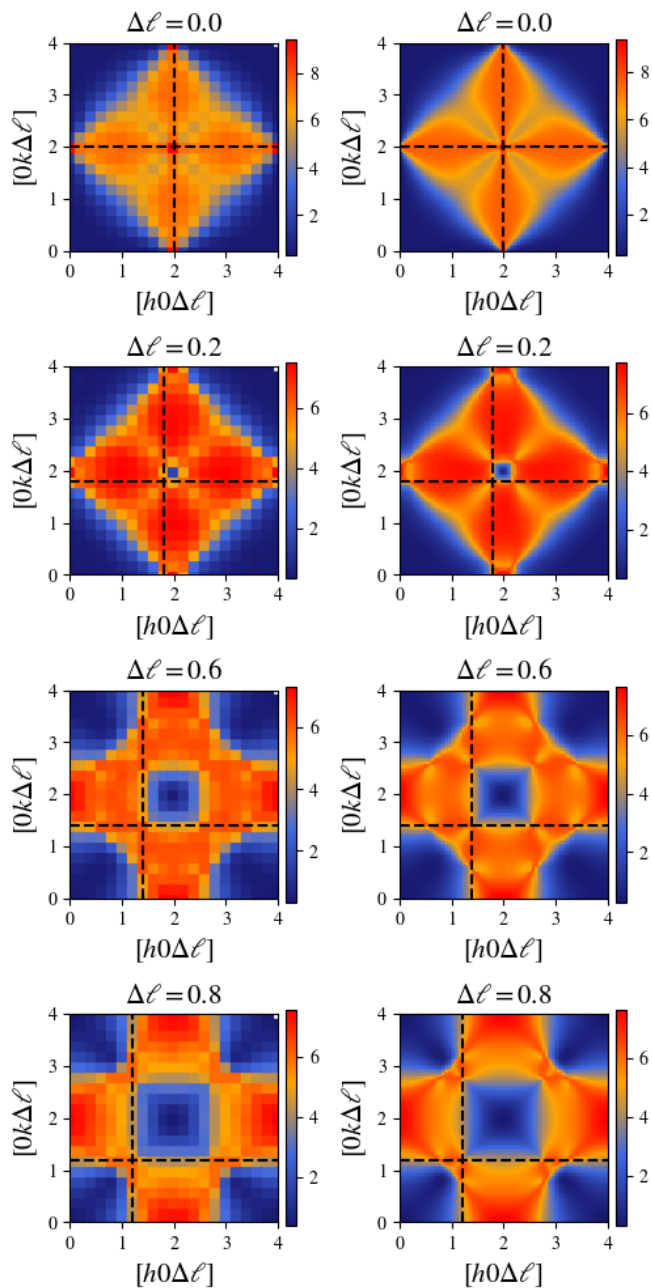


FIG. 9. Spin structure factors obtained via classical Monte Carlo simulations at  $T = 0.03|J_{zz}|$  (left column) and large- $\mathcal{N}$  approximation in the  $T \rightarrow 0$  limit (right column) for the CSL 6 at various reciprocal plane cuts  $[hk\Delta\ell]$ , where the value of  $\Delta\ell$  is specified at the top of each panel. Here, the black dashed lines are drawn at  $h = 2 - \Delta\ell$  and  $k = 2 - \Delta\ell$ . The intersection of these lines marks the  $\Delta\ell \times [11\bar{1}]$  direction which tracks the location of the pinch lines where two-fold pinch points are observed.

breaking transition down to the lowest temperatures where it plateaus to a value around the theoretical value  $3/4$  [59, 92]. As in the HAFM, the spin structure factor of the HAFM\* exposes two-fold pinch points, as seen in

the  $[hk0]$  scattering plane both in CMC and predicted by large- $\mathcal{N}$ . We further note that the structure factor of the HAFM\* appears as an intensity-inverted version of that of the HAFM. In other words, the regions of high intensity in the spin structure factor of one model correspond to regions of low intensity in the dual model.

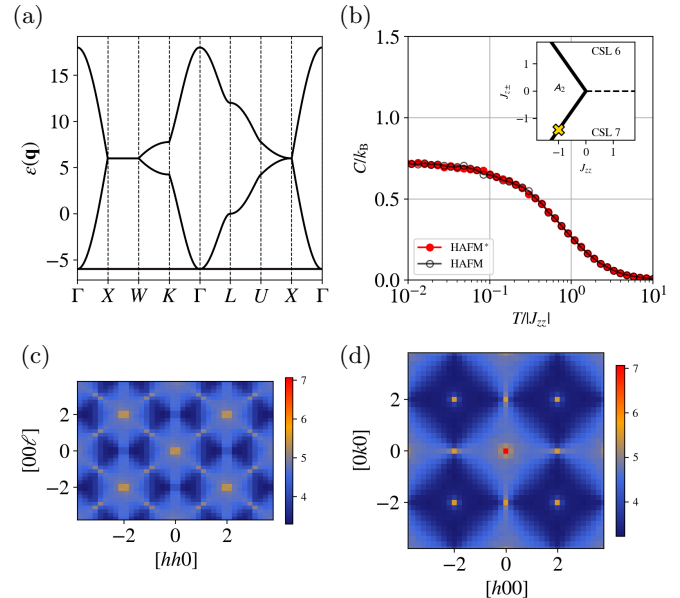


FIG. 10. (a) Interaction matrix bands, (b) specific heat, and structure factors in the  $[h\ell\ell]$  (c) and  $[hk0]$  (d) planes of the CSL9, the HAFM\* model. (a) Diagonalized interaction matrix [Eq. (5)] band in reciprocal space for CSL 9 (HAFM\*), using parameters  $\{J_{zz}, J_{\pm}, J_{\pm\pm}, J_{z\pm}\} = \{-1.0, 0.5, 1, -\sqrt{2}\}$ . There are six flat bands at the bottom of the spectrum and the dispersive bands are three-fold degenerate. The spectrum is identical to that of CSL 8 (HAFM) due to the duality of Eq. (59) between the two models. (b) Specific heat of the HAFM\* and HAFM model, showing no sharp phase transitions from the paramagnetic phase down to the lowest temperature. The inset in this figure shows the precise location of the model in the phase diagram shown in Fig. 5. (c,d) neutron structure factors in the  $[h\ell\ell]$  and  $[hk0]$  planes of the model. Although CSL 8 and CSL 9 are dual to each other, their spin structure factor is different.

## VIII. THE UNSUCCESSFUL CSL CANDIDATES

In this section, we briefly discuss the unsuccessful CSL candidates that sit on the boundaries between three magnetically ordered phases yet present a symmetry-breaking transition at low temperatures. So far we have provided a list of the CSLs stable down to the lowest temperatures and therefore lack any type of conventional symmetry-breaking transition. In the large- $\mathcal{N}$  approximation, a CSL is realized whenever the lowest band (or bands) of

the interaction matrix is flat, resulting in an extensive degeneracy in the ground states. The extensive degeneracy associated with low-energy flat bands in the large- $\mathcal{N}$  approximation, however, does not impede the onset of an order-by-disorder selection of a symmetry-breaking spin configuration. Such entropically driven selection mechanisms are typically described by high-order terms in the free energy which are not captured by the large- $\mathcal{N}$  approximation [62]. Consequently, the stability of a CSL must be tested using CMC.

It turns out that, broadly speaking, these models are located at the three edges of the green pyramid of the  $A_2$  phase (all-in-all-out magnetic order) Fig. 2(a) and Fig. 3 for the non-Kramers and Kramers Hamiltonian, respectively. We refer to the models defined on these edges by the minimal irreps describing their ground states, namely,  $A_2 \oplus T_{1,p} \oplus T_2$  [82],  $A_2 \oplus E \oplus T_2$ , and  $A_2 \oplus E \oplus T_{1,p}$  for the non-Kramers case and the same labeling but replacing  $T_{1,p}$  by  $T_{1,-}$  for the Kramers case.

An analysis of the large- $\mathcal{N}$  interaction matrix bands for the non-Kramers Hamiltonian models reveals that the  $A_2 \oplus T_{1,p} \oplus T_2$  model possesses four low-energy flat bands in its interaction matrix spectrum, whereas both the  $A_2 \oplus E \oplus T_2$  and the  $A_2 \oplus E \oplus T_{1,p}$  models yield two low-energy flat bands. On the other hand, for the Kramers models, both the  $A_2 \oplus T_{1,-} \oplus T_2$  model and the  $A_2 \oplus E \oplus T_2$  yield two low-energy flat bands, while the  $A_2 \oplus E \oplus T_{1,-}$  has no flat bands in its interaction matrix spectrum. As previously mentioned, all of these models (with the exception of the  $A_2 \oplus E \oplus T_{1,-}$  Kramers model) are predicted to be a CSL according to the large- $\mathcal{N}$  analysis. However, a detailed CMC analysis of these reveals that all of them undergo a symmetry-breaking phase transition at low temperatures (not shown in this paper). We leave the study of details of these unsuccessful CSL candidates for future work.

Lastly, we note that the CSLs listed in Table I and the unsuccessful CSL candidates discussed in this section constitute all the triple-phase boundary regions (with the exception of the CSL 1 (spin ice) and the CSL 2 ( $SL_{\perp}$ ) phases) in the interaction parameter space  $\{J_{zz}, J_{\pm}, J_{\pm\pm}, J_{z\pm}\}$  of the most generic nearest-neighbor Hamiltonian in the pyrochlore lattice. In a similar spirit, we also examined all boundaries separating two magnetic ordered phases, with the only CSL that we discovered being the CSL 2 that lives on the boundary of  $T_{1,p}$  and  $T_2$  magnetic orders. We thus have exhausted all potential parameter spaces supporting CSLs, and the list of CSLs for this general pyrochlore Hamiltonian is thus complete.

## IX. DISCUSSION AND CONCLUSION

Our work provides a comprehensive atlas of CSLs that are realized on the pyrochlore lattice and have developed a theory of inter-tetrahedra constraints in terms of irreducible representation fields. In doing so, we identified the parameter spaces parameterizing all possible CSLs for the nearest-neighbor anisotropic spin Hamiltonian on

the pyrochlore lattice. We have constructed effective gauge field theories for these CSLs and have explained how the CSLs are connected or transform into each other. Our results, summarized in Table I and Figs. 2, 3, 5, include 9 distinct spin liquids described by various effective long-wavelength theories characterized by the emergence of energetically imposed Gauss-like law constraints. In aiming to obtain support for the field theory picture and to understand these systems quantitatively at the microscopic level, we also performed large- $\mathcal{N}$  self-consistent Gaussian approximation (SCGA) and classical Monte Carlo (CMC) simulations.

Within the spin-spin couplings arising in the Hamiltonian of Eq. (1), the list of CSLs on the pyrochlore lattice is *exhaustive*. Referring to Figs. 2, 3, one notes that we have scanned all boundaries of two and three long-range ordered phases as well as the classically disordered spin ice phase. Therefore, we are confident that there remains no other CSLs to be discovered in the phase diagram. By following our methodology to implement inter-tetrahedra constraints, and using CMC simulations, it would be straightforward to discover CSLs hosted by other anisotropic pyrochlore Hamiltonians. For example, one could consider other couplings such as the single-ion anisotropy term  $D$  in Eq. (3) and long-range dipole-dipole interactions, as long as the long-range ordered phase considered have a  $= 0$  propagation vector. Extending our theory to CSLs stabilized by interactions beyond nearest neighbors [99, 100] as well as the breathing pyrochlore model [101] would also be an interesting line of study to pursue.

In this work, we have identified two new spin liquid phases and are given in the compiled list of CSLs in Table I. Specifically, these are CSL 6 (as scalar-vector-charge R2U1, or SV R2U1), which is dual to the pinch-line spin liquid, and the CSL 9 as a dual to the Heisenberg antiferromagnet (HAFM\*). Although these two are dual to previously discovered CSLs, their spin couplings and structure factor are different. The physical consequence of infinitely many charge-conservation laws for CSLs 6 and 7 that we noted in the present work is an interesting question awaiting further analysis.

From the work presented here, we now have a comprehensive overview of all the CSLs on the pyrochlore lattice and how these transform into each other as a consequence of modifying the lowest degenerate irreps by varying the anisotropic bilinear spin-spin couplings. Such insight is crucial for understanding the exotic physics of anisotropic spin models on the pyrochlore lattice, especially for materials that happen to be finding themselves near the phase boundaries of pseudospin long-range order [15, 52, 53, 70–72]. Our result provides crucial information for guiding the ultimate construction of a similar atlas for the quantum model, by exploring parameter space identified in this work, akin to what has been done in Ref. [62]. Our atlas of CSLs on the pyrochlore lattice with nearest-neighbor couplings is a crucial step toward complete understanding of the most representative frus-

trated magnet.

## ACKNOWLEDGMENTS

The authors acknowledge useful discussions with Ludovic Jaubert, Nic Shannon, Roderich Moessner, Yasir Iqbal, Rajiv Singh, Jaan Oitma Johannes Reuther, Andriy Nevidomskyy, Kristian Chung, and Matthias Vojta. D. L.-G. acknowledges financial support from the DFG through the Hallwachs-Röntgen Postdoc Program of the Würzburg-Dresden Cluster of Excellence on Complexity and Topology in Quantum Matter – *ct.qmat* (EXC 2147, project-id 390858490) and through SFB 1143 (project-id 247310070). H.Y. acknowledges the 2024 Toyota Riken Scholar Program from the Toyota Physical and Chemical Research Institute, and the Grant-in-Aid for Research Activity Start-up from Japan Society for the Promotion of Science (Grant No. 24K22856). The work at the University of Waterloo was supported by the NSERC of Canada and the Canada Research Chair (Tier 1, M.J.P.G.) program.

## Appendix A: Hamiltonian in the physical and global spin basis

In this appendix, we provide an alternative basis for the general bilinear nearest-neighbor Hamiltonian in the pyrochlore lattice in Eq. (1) [51]. Doing so will further emphasize how the form of the spin Hamiltonian appears significantly different when considering the dual forms discussed above. The Hamiltonian can be parametrized in what we refer to as a “spin vector interaction” basis (SVI) basis with Heisenberg  $J$ , local Ising  $J_{\text{Ising}}$ , pseudo-dipole  $J_{\text{PD}}$ , and Dzyaloshinskii-Moriya (DM)  $J_{\text{DM}}$  interactions. This SVI basis, the Hamiltonian in Eq (1) reads

$$\mathcal{H} = \mathcal{H}_{\text{Heis}} + \mathcal{H}_{\text{Ising}} + \mathcal{H}_{\text{PD}} + \mathcal{H}_{\text{DM}} \quad (\text{A1})$$

$$\mathcal{H}_{\text{Heis}} = J \sum_{\langle ij \rangle} \mathbf{S}_i \cdot \mathbf{S}_j \quad (\text{A2})$$

$$\mathcal{H}_{zz} = J_{\text{Ising}} \sum_{\langle ij \rangle} (\mathbf{S}_i \cdot \mathbf{z}_i) (\mathbf{S}_j \cdot \mathbf{z}_j) \quad (\text{A3})$$

$$\mathcal{H}_{\text{PD}} = J_{\text{PD}} \sum_{\langle ij \rangle} (\mathbf{S}_i \cdot \mathbf{r}_{ij}) (\mathbf{r}_{ij} \cdot \mathbf{S}_j) \quad (\text{A4})$$

$$\mathcal{H}_{\text{DM}} = J_{\text{DM}} \sum_{\langle ij \rangle} \mathbf{d}_{ij} \cdot (\mathbf{S}_i \times \mathbf{S}_j), \quad (\text{A5})$$

where the spins  $\mathbf{S}_i$  are here defined in the global Cartesian basis,  $\mathbf{z}_i$  is the local- $z$  (cubic [111]) direction at the  $i$ th lattice site,  $\mathbf{r}_{ij}$  is the separation vector between lattices sites  $i$  and  $j$ , and  $\mathbf{d}_{ij}$  labels the direct DM vectors as defined in Ref. [102]. The relation between the interaction parameters basis  $\{J_{zz}, J_{\pm}, J_{\pm\pm}, J_{z\pm}\}$  and the above

$\{J, J_{\text{Ising}}, J_{\text{PD}}, J_{\text{DM}}\}$  basis yields

$$J = 2(J_{\pm} + J_{\pm\pm}), \quad (\text{A6})$$

$$J_{\text{Ising}} = -10J_{\pm} - 2J_{\pm\pm} + 4\sqrt{2}J_{z\pm} + J_{zz}, \quad (\text{A7})$$

$$J_{\text{PD}} = -4(2J_{\pm} + J_{\pm\pm} - \sqrt{2}J_{z\pm}), \quad (\text{A8})$$

$$J_{\text{DM}} = -4J_{\pm} + \sqrt{2}J_{z\pm}. \quad (\text{A9})$$

Consider now the duality between CSL 8 and CSL 9 that is generated upon the change of sign of  $J_{z\pm}$ . In SVI basis, the former is simply an antiferromagnetic Heisenberg model, namely  $\{J, J_{\text{Ising}}, J_{\text{PD}}, J_{\text{DM}}\} = \{\frac{3}{\sqrt{2}}J_{z\pm}, 0, 0, 0\}$ , while the CSL 9 is a model where all parameters in the SVI basis are non-vanishing, i.e.  $\{J, J_{\text{Ising}}, J_{\text{PD}}, J_{\text{DM}}\} = \{-\frac{3}{\sqrt{2}}J_{z\pm}, 8\sqrt{2}J_{z\pm}, 8\sqrt{2}J_{z\pm}, 2\sqrt{2}J_{z\pm}\}$ .

We further note that, in addition to the local basis, i.e.  $\{J_{zz}, J_{\pm}, J_{\pm\pm}, J_{z\pm}\}$ , and the SVI basis,  $\{J, J_{\text{Ising}}, J_{\text{PD}}, J_{\text{DM}}\}$ , a global parameter basis, namely  $\{J_1, J_2, J_3, J_4\}$  is also extensively used in the literature. In the global basis, the spin components are expressed in global Cartesian coordinates, and the spin Hamiltonian takes the form

$$H_{\text{ex}} = \sum_{\langle ij \rangle} \mathbf{S}_i \cdot \mathcal{J}_{ij} \cdot \mathbf{S}_j, \quad (\text{A10})$$

where the exchange matrix  $\mathcal{J}_{ij}$  couples the spins in the  $i$  and  $j$  sites. For instance for the sublattices 0 and 1 this exchange matrix takes the form

$$\mathcal{J}_{01} = \begin{pmatrix} J_2 & J_4 & J_4 \\ -J_4 & J_1 & J_3 \\ -J_4 & J_3 & J_1 \end{pmatrix}, \quad (\text{A11})$$

while all other exchange matrices can be obtained by applying the transformation of the single tetrahedron group  $T_d$ . For the explicit form of these exchange matrices we refer the reader to Ref. [53]. The relationship between the local and the global basis is given by the transformation

$$J_1 = \frac{1}{3} \left( -J_{zz} + 4J_{\pm} + 2J_{\pm\pm} + 2\sqrt{2}J_{z\pm} \right), \quad (\text{A12})$$

$$J_2 = \frac{1}{3} \left( J_{zz} - 4J_{\pm} + 4J_{\pm\pm} + 4\sqrt{2}J_{z\pm} \right), \quad (\text{A13})$$

$$J_3 = \frac{1}{3} \left( -J_{zz} - 2J_{\pm} - 4J_{\pm\pm} + 2\sqrt{2}J_{z\pm} \right), \quad (\text{A14})$$

$$J_4 = \frac{1}{3} \left( -J_{zz} - 2J_{\pm} + 2J_{\pm\pm} - \sqrt{2}J_{z\pm} \right). \quad (\text{A15})$$

In the global basis, the parametrization of the CSL 8 and 9 is given by  $\{J_1, J_2, J_3, J_4\} = \{\frac{3J_{z\pm}}{\sqrt{2}}, \frac{3J_{z\pm}}{\sqrt{2}}, 0, 0\}$  and  $\{J_1, J_2, J_3, J_4\} = \{-\frac{J_{z\pm}}{3\sqrt{2}}, \frac{7J_{z\pm}}{3\sqrt{2}}, \frac{4\sqrt{2}J_{z\pm}}{3}, -\frac{2\sqrt{2}J_{z\pm}}{3}\}$ , respectively.

## Appendix B: Irreducible representations and their exchange coefficients in the global basis

In the main text, we discussed the degeneracy of different magnetic orders using the irrep description with

the spin degrees of freedom expressed in the local basis. In this appendix, we provide the irrep modes  $\{\mathbf{m}_X\}$  in the global Cartesian basis as well as their exchange coefficients,  $a_X$ , in the global and in SVI basis above. In Table IV gives the the irrep modes in terms of the spin DOFs defined in the global basis while Table V gives the exchange coefficients,  $a_X$ , in terms of the global and SVI basis.

### Appendix C: Correlation functions

In this appendix, we give the expressions for the correlation functions presented in the main text. In reciprocal space, and for a generic non-Bravais lattice with a sublattice structure, the general correlation between spins is given by the expression

$$S_{\mu\nu}^{\alpha\gamma} = \langle S_\mu^\alpha(\mathbf{q}) S_\nu^\gamma(-\mathbf{q}) \rangle, \quad (\text{C1})$$

where  $\mu, \nu$  label the sublattice position and  $\alpha, \beta$  the spin components. In particular, we compute the additive contribution of the spin-component diagonal elements of the general correlation function

$$\begin{aligned} \mathcal{S}(\mathbf{q}) &= \sum_\alpha \sum_{\mu, \nu} S_{\mu\nu}^{\alpha\alpha} \\ &= \sum_\alpha \sum_{\mu, \nu} \langle S_\mu^\alpha(\mathbf{q}) S_\nu^\alpha(-\mathbf{q}) \rangle, \end{aligned} \quad (\text{C2})$$

which for simplicity we refer to as the spin structure factor. The experimentally measurable unpolarized neutron structure factor is given by

$$S_\perp(\mathbf{q}) = \sum_{\alpha, \beta} \sum_{\mu, \nu} \left( \delta_{\alpha, \beta} - \hat{\mathbf{q}}^\alpha \hat{\mathbf{q}}^\beta \right) \langle S_\mu^\alpha(\mathbf{q}) S_\nu^\beta(-\mathbf{q}) \rangle, \quad (\text{C3})$$

and the polarized neutron structure factor defined in terms of the incident neutrons' polarization  $\hat{z}_N$  [103] This polarization analysis separates the neutron structure factor into two channels, the non-spin-flip (NSF) channel which studies the correlations that are parallel to the incident polarization  $\hat{z}_N$

$$S_\perp^{\text{NSF}}(\mathbf{q}) = \sum_{\alpha, \gamma} \sum_{\mu, \nu} (\hat{z}_N^\alpha \hat{z}_N^\gamma) \langle S_\mu^\alpha S_\nu^\gamma \rangle, \quad (\text{C4})$$

and the spin-flip channel which is the complement of the NSF channel, defined as

$$S_\perp^{\text{SF}}(\mathbf{q}) = S_\perp(\mathbf{q}) - S_\perp^{\text{NSF}}(\mathbf{q}). \quad (\text{C5})$$

In this work we have assumed that the spin degrees of freedom  $\mathbf{S}_{i\mu}$  correspond to the magnetic moments,  $\mathbf{m}_{i\mu}$ , of the systems considered where the sub-index  $i$  labels the primitive FCC vectors  $\mathbf{R}_i$  and  $\mu$  denotes the sublattice basis. However, in real materials [14–16], the relation between these two quantities is provided by an anisotropic  $g$ -tensor

$$m_{i\mu}^\alpha = \sum_\beta g_\mu^{\alpha\beta} S_{i\mu}^\beta, \quad (\text{C6})$$

where  $g_\mu^{\alpha\beta}$  are the components of the  $g$ -tensor associated to the  $\mu$ -sublattice. The introduction of an anisotropic  $g$ -tensor however would “distort” in momentum ( $q$ ) space the correlation functions we have presented [62, 94, 95] which were considered to discernibly expose the underlying gauge theory and the analysis performed intact. For this reason, when reporting in the main text neutron structure factors (e.g. see Fig. 6), we chose an isotropic  $g$ -tensor (i.e.  $g_\mu^{\alpha\beta} = g\delta_{\alpha\beta}$ ). To reiterate, in doing so, we make no assumptions on the nature (Kramers or non-Kramers) of the spin degrees of freedom in order to more clearly expose the underlying gauge theory of the CSLs considered.

### Appendix D: Large- $\mathcal{N}$

The large- $\mathcal{N}$  approximation, also known as the self-consistent Gaussian approximation (SCGA) is a classical approximation where the hard spin length constraint on the spin  $|\mathbf{S}_i|^2 = S^2$  is replaced by a soft spin length constraint  $\langle |\mathbf{S}_i|^2 \rangle = S^2$  which is energetically imposed by means of an introduced Lagrange multiplier  $\lambda$ . This approximation results in a Gaussian theory which can be exactly solved [104–107]. In this appendix we provide a minimal introduction to this approximation.

We first consider the generic bilinear Hamiltonian in Eq. (1), which can be written as

$$\mathcal{H} = \frac{1}{2} \sum_{i\mu, j\nu} \sum_{\alpha, \gamma} S_{i\mu}^\alpha \mathbf{J}_{i\mu, j\nu}^{\alpha, \gamma} S_{j\nu}^\gamma, \quad (\text{D1})$$

where the sub-indices  $i$  and  $j$  label the primitive FCC vectors  $\mathbf{R}_i$  and  $\mu$  and  $\nu$  denote the sublattice basis. The generic spin-spin correlation function in  $q$  space is given by

$$S_{\mu\nu}^{\alpha\gamma} = \langle S_\mu^\alpha(\mathbf{q}) S_\nu^\gamma(-\mathbf{q}) \rangle = \sum_{\mathbf{q}} (\beta \mathbf{J}_{\mu\nu}^{\alpha\gamma}(\mathbf{q}) + \lambda)^{-1}, \quad (\text{D2})$$

where the Lagrange multiplier  $\lambda$  is determined self consistently at every temperature  $T = 1/\beta$  by solving the equation

$$S^2 = \frac{1}{N} \sum_{m, \mathbf{q}} (\beta \varepsilon_m(\mathbf{q}) + \lambda)^{-1}, \quad (\text{D3})$$

where  $\varepsilon_m(\mathbf{q})$  corresponds to the  $m$ -th eigenvalue of the interaction matrix  $\mathbf{J}_{i\mu, j\nu}^{\alpha, \gamma}$  expressed in momentum space,  $\mathbf{J}_{\mu\nu}^{\alpha\gamma}(\mathbf{q})$ .

TABLE IV. Relation between irreducible representations of the point group and the spins in the global basis.

Local order parameter field	Definition in terms of spin components
$m_{A_2}$	$\frac{1}{\sqrt{3}}(S_0^x + S_0^y + S_0^z + S_1^x - S_1^y - S_1^z - S_2^x + S_2^y - S_2^z - S_3^x - S_3^y + S_3^z)$
$\mathbf{m}_E$	$\left( \begin{array}{c} \frac{1}{\sqrt{6}}(-2S_0^x + S_0^y + S_0^z - 2S_1^x - S_1^y - S_1^z + 2S_2^x + S_2^y - S_2^z + 2S_3^x - S_3^y + S_3^z) \\ \frac{1}{\sqrt{2}}(-S_0^y + S_0^z + S_1^y - S_1^z - S_2^y - S_2^z + S_3^y + S_3^z) \end{array} \right)$
$\mathbf{m}_{T_2}$	$\left( \begin{array}{c} \frac{1}{\sqrt{2}}(-S_0^y + S_0^z + S_1^y - S_1^z + S_2^y + S_2^z - S_3^y - S_3^z) \\ \frac{1}{\sqrt{2}}(S_0^x - S_0^z - S_1^x - S_1^z - S_2^x + S_2^z + S_3^x + S_3^z) \\ \frac{1}{\sqrt{2}}(-S_0^x + S_0^y + S_1^x + S_1^y - S_2^x - S_2^y + S_3^x - S_3^y) \end{array} \right)$
$\mathbf{m}_{T_{1,i}}$	$\left( \begin{array}{c} \frac{1}{\sqrt{3}}(S_0^x + S_0^y + S_0^z + S_1^x - S_1^y - S_1^z + S_2^x - S_2^y + S_2^z + S_3^x + S_3^y - S_3^z) \\ \frac{1}{\sqrt{3}}(S_0^x + S_0^y + S_0^z - S_1^x + S_1^y + S_1^z - S_2^x + S_2^y - S_2^z + S_3^x + S_3^y - S_3^z) \\ \frac{1}{\sqrt{3}}(S_0^x + S_0^y + S_0^z - S_1^x + S_1^y + S_1^z + S_2^x - S_2^y + S_2^z - S_3^x - S_3^y + S_3^z) \end{array} \right)$
$\mathbf{m}_{T_{1,p}}$	$\left( \begin{array}{c} \frac{1}{\sqrt{6}}(-2S_0^x + S_0^y + S_0^z - 2S_1^x - S_1^y - S_1^z - 2S_2^x - S_2^y + S_2^z - 2S_3^x + S_3^y - S_3^z) \\ \frac{1}{\sqrt{6}}(S_0^x - 2S_0^y + S_0^z - S_1^x - 2S_1^y + S_1^z - S_2^x - 2S_2^y - S_2^z + S_3^x - 2S_3^y - S_3^z) \\ \frac{1}{\sqrt{6}}(S_0^x + S_0^y - 2S_0^z - S_1^x + S_1^y - 2S_1^z + S_2^x - S_2^y - 2S_2^z - S_3^x - S_3^y - 2S_3^z) \end{array} \right)$

TABLE V. Coefficients of the irreducible representations used in Eq. (3) and Eq. (A1)

Coefficient	Definition in terms of exchange parameters $\{J_1, J_2, J_3, J_4, D\}$	Definition in terms of exchange parameters $\{J, J_{\text{Ising}}, J_{\text{PD}}, J_{\text{DM}}, D\}$
$a_{A_2}$	$-2J_1 + J_2 - 2(J_3 + 2J_4) + D$	$-J - 4J_{\text{DM}} + 3J_{\text{Ising}} + D$
$a_E$	$-2J_1 + J_2 + J_3 + 2J_4$	$\frac{1}{2}(-2J + 4J_{\text{DM}} - J_{\text{PD}})$
$a_{T_2}$	$-J_2 + J_3 - 2J_4$	$\frac{1}{2}(-2J - 4J_{\text{DM}} + J_{\text{PD}})$
$a_{T_1 \text{ ice}}$	$\frac{1}{3}(2J_1 - J_2 + 2J_3 + 4J_4) + D$	$\frac{1}{3}(J + 4J_{\text{DM}} - 3J_{\text{Ising}} + 2J_{\text{PD}}) + D$
$a_{T_1 \text{ planar}}$	$\frac{1}{3}(4J_1 + J_2 - 5J_3 + 2J_4)$	$\frac{1}{6}(10J + 4J_{\text{DM}} - J_{\text{PD}})$
$a_{T_1 \text{ mixing}}$	$-\frac{4\sqrt{2}}{3}(J_1 + J_2 + J_3 - J_4)$	$-\frac{4\sqrt{2}}{3}(2J - J_{\text{DM}} + J_{\text{PD}})$

- [1] X.-G. Wen, *Quantum Field Theory of Many-Body Systems* (Oxford University Press, 2007).
- [2] L. Balents, Spin liquids in frustrated magnets, *Nature* **464**, 199 (2010).
- [3] C. Lacroix, P. Mendels, and F. Mila, *Introduction to Frustrated Magnetism* (Springer, 2011).
- [4] Y. Zhou, K. Kanoda, and T.-K. Ng, Quantum spin liquid states, *Rev. Mod. Phys.* **89**, 025003 (2017).
- [5] L. Savary and L. Balents, Quantum spin liquids: A review, *Rep. Prog. Phys.* **80**, 016502 (2016).
- [6] M. J. P. Gingras and P. A. McClarty, Quantum spin ice: a search for gapless quantum spin liquids in pyrochlore magnets, *Reports on Progress in Physics* **77**, 056501 (2014).
- [7] J. Knolle and R. Moessner, A field guide to spin liquids, *Annu. Rev. Condens. Matter Phys.* **10**, 451 (2019).
- [8] R. Moessner and J. E. Moore, *Topological Phases of Matter* (Cambridge University Press, 2021).
- [9] H. Yan, O. Benton, R. Moessner, and A. H. Nevidomskyy, Classification of classical spin liquids: Typology and resulting landscape, *Phys. Rev. B* **110**, L020402 (2024).
- [10] H. Yan, O. Benton, A. H. Nevidomskyy, and R. Moessner, Classification of classical spin liquids: Detailed formalism and suite of examples, *Phys. Rev. B* **109**, 174421 (2024).
- [11] Y. Fang, J. Cano, A. H. Nevidomskyy, and H. Yan, Classification of classical spin liquids: Topological quantum chemistry and crystalline symmetry, *Phys. Rev. B* **110**, 054421 (2024).
- [12] D. L. Bergman, C. Wu, and L. Balents, Band touching from real-space topology in frustrated hopping models, *Phys. Rev. B* **78**, 125104 (2008).
- [13] J. Villain, R. Bidaux, J.-P. Carton, and R. Conte, Order as an effect of disorder, *J. Phys. France*, **41**, 1263 (1980).
- [14] J. S. Gardner, M. J. P. Gingras, and J. E. Greedan, Magnetic pyrochlore oxides, *Rev. Mod. Phys.* **82**, 53 (2010).
- [15] A. M. Hallas, J. Gaudet, and B. D. Gaulin, Experimental insights into ground-state selection of quantum xy pyrochlores, *Annu. Rev. Condens. Matter Phys.* **9**, 105 (2018).
- [16] J. G. Rau and M. J. Gingras, Frustrated quantum rare-earth pyrochlores, *Annual Review of Condensed Matter Physics* **10**, 357 (2019).

- [17] M. J. Harris, S. T. Bramwell, D. F. McMorrow, T. Zeiske, and K. W. Godfrey, Geometrical frustration in the ferromagnetic pyrochlore  $\text{Ho}_2\text{Ti}_2\text{O}_7$ , *Phys. Rev. Lett.* **79**, 2554 (1997).
- [18] S. T. Bramwell and M. J. P. Gingras, Spin ice state in frustrated magnetic pyrochlore materials, *Science* **294**, 1495 (2001).
- [19] C. Castelnovo, R. Moessner, and S. Sondhi, Spin Ice, Fractionalization, and Topological Order, *Annual Review of Condensed Matter Physics* **3**, 35 (2012).
- [20] M. Udagawa and L. Jaubert, eds., *Spin Ice*, Springer Series in Solid-State Sciences, Vol. 197 (Springer International Publishing, Cham, 2021).
- [21] S. T. Bramwell, M. J. Harris, B. C. den Hertog, M. J. P. Gingras, J. S. Gardner, D. F. McMorrow, A. R. Wildes, A. L. Cornelius, J. D. M. Champion, R. G. Melko, and T. Fennell, Spin correlations in  $\text{Ho}_2\text{Ti}_2\text{O}_7$ : A dipolar spin ice system, *Phys. Rev. Lett.* **87**, 047205 (2001).
- [22] T. Fennell, O. A. Petrenko, B. Fåk, J. S. Gardner, S. T. Bramwell, and B. Ouladdiaf, Neutron scattering studies of the spin ices  $\text{Ho}_2\text{Ti}_2\text{O}_7$  and  $\text{Dy}_2\text{Ti}_2\text{O}_7$  in applied magnetic field, *Phys. Rev. B* **72**, 224411 (2005).
- [23] T. Fennell, P. P. Deen, A. R. Wildes, K. Schmalzl, D. Prabhakaran, A. T. Boothroyd, R. J. Aldus, D. F. McMorrow, and S. T. Bramwell, Magnetic Coulomb phase in the Spin Ice  $\text{Ho}_2\text{Ti}_2\text{O}_7$ , *Science* **326**, 415 (2009).
- [24] T. Fennell, O. A. Petrenko, B. Fåk, S. T. Bramwell, M. Enjalran, T. Yavors'kii, M. J. P. Gingras, R. G. Melko, and G. Balakrishnan, Neutron scattering investigation of the spin ice state in  $\text{Dy}_2\text{Ti}_2\text{O}_7$ , *Phys. Rev. B* **70**, 134408 (2004).
- [25] D. J. P. Morris, D. A. Tennant, S. A. Grigera, B. Klemke, C. Castelnovo, R. Moessner, C. Czternasty, M. Meissner, K. C. Rule, J.-U. Hoffmann, K. Kiefer, S. Gerischer, D. Slobinsky, and R. S. Perry, Dirac strings and magnetic monopoles in the spin ice  $\text{Dy}_2\text{Ti}_2\text{O}_7$ , *Science* **326**, 411 (2009).
- [26] C. Castelnovo, R. Moessner, and S. L. Sondhi, Magnetic monopoles in spin ice, *Nature* **451**, 42 (2008).
- [27] J. G. Rau and M. J. P. Gingras, Magnitude of quantum effects in classical spin ices, *Phys. Rev. B* **92**, 144417 (2015).
- [28] H. D. Zhou, J. G. Cheng, A. M. Hallas, C. R. Wiebe, G. Li, L. Balicas, J. S. Zhou, J. B. Goodenough, J. S. Gardner, and E. S. Choi, Chemical pressure effects on pyrochlore spin ice, *Phys. Rev. Lett.* **108**, 207206 (2012).
- [29] M. Hermele, M. P. A. Fisher, and L. Balents, Pyrochlore photons: The  $u(1)$  spin liquid in a  $s = \frac{1}{2}$  three-dimensional frustrated magnet, *Phys. Rev. B* **69**, 064404 (2004).
- [30] H. R. Molavian, M. J. P. Gingras, and B. Canals, Dynamically induced frustration as a route to a quantum spin ice state in  $\text{Tb}_2\text{Ti}_2\text{O}_7$  via virtual crystal field excitations and quantum many-body effects, *Phys. Rev. Lett.* **98**, 157204 (2007).
- [31] S. Onoda and Y. Tanaka, Quantum melting of spin ice: Emergent cooperative quadrupole and chirality, *Phys. Rev. Lett.* **105**, 047201 (2010).
- [32] S. Lee, S. Onoda, and L. Balents, Generic quantum spin ice, *Phys. Rev. B* **86**, 104412 (2012).
- [33] O. Benton, O. Sikora, and N. Shannon, Seeing the light: Experimental signatures of emergent electromagnetism in a quantum spin ice, *Phys. Rev. B* **86**, 075154 (2012).
- [34] N. Shannon, O. Sikora, F. Pollmann, K. Penc, and P. Fulde, Quantum Ice: A Quantum Monte Carlo Study, *Physical Review Letters* **108**, 067204 (2012).
- [35] C.-J. Huang, Y. Deng, Y. Wan, and Z. Y. Meng, Dynamics of topological excitations in a model quantum spin ice, *Phys. Rev. Lett.* **120**, 167202 (2018).
- [36] O. Benton, Ground-state phase diagram of dipolar-octupolar pyrochlores, *Phys. Rev. B* **102**, 104408 (2020).
- [37] S. D. Pace, S. C. Morampudi, R. Moessner, and C. R. Laumann, Emergent fine structure constant of quantum spin ice is large, *Phys. Rev. Lett.* **127**, 117205 (2021).
- [38] M. Hosoi, E. Z. Zhang, A. S. Patri, and Y. B. Kim, Uncovering Footprints of Dipolar-Octupolar Quantum Spin Ice from Neutron Scattering Signatures, *Physical Review Letters* **129**, 097202 (2022).
- [39] F. Desrochers and Y. B. Kim, Spectroscopic signatures of fractionalization in octupolar quantum spin ice, *Phys. Rev. Lett.* **132**, 066502 (2024).
- [40] H. Yan, A. Sanders, C. Castelnovo, and A. H. Nevidomskyy, Experimentally tunable qed in dipolar-octupolar quantum spin ice, arXiv:2312.11641 10.48550/arXiv.2312.11641 (2023).
- [41] K. Kimura, S. Nakatsuji, J.-J. Wen, C. Broholm, M. B. Stone, E. Nishibori, and H. Sawa, Quantum fluctuations in spin-ice-like  $\text{Pr}_2\text{Zr}_2\text{O}_7$ , *Nature Communications* **4**, 1934 (2013).
- [42] R. Sibille, N. Gauthier, H. Yan, M. Ciomaga Hatnean, J. Ollivier, B. Winn, U. Filges, G. Balakrishnan, M. Kenzelmann, N. Shannon, and T. Fennell, Experimental signatures of emergent quantum electrodynamicism in  $\text{Pr}_2\text{Hf}_2\text{O}_7$ , *Nature Physics* **14**, 711 (2018).
- [43] B. Gao, T. Chen, D. W. Tam, C.-L. Huang, K. Sasmal, D. T. Adroja, F. Ye, H. Cao, G. Sala, M. B. Stone, C. Baines, J. A. T. Verezhak, H. Hu, J.-H. Chung, X. Xu, S.-W. Cheong, M. Nallaiyan, S. Spagna, M. B. Maple, A. H. Nevidomskyy, E. Morosan, G. Chen, and P. Dai, Experimental signatures of a three-dimensional quantum spin liquid in effective spin-1/2  $\text{Ce}_2\text{Zr}_2\text{O}_7$  pyrochlore, *Nature Physics* **15**, 1052 (2019).
- [44] J. Gaudet, E. M. Smith, J. Dudemaine, J. Beare, C. R. C. Buhariwalla, N. P. Butch, M. B. Stone, A. I. Kolesnikov, G. Xu, D. R. Yahne, K. A. Ross, C. A. Marjerrison, J. D. Garrett, G. M. Luke, A. D. Bianchi, and B. D. Gaulin, Quantum spin ice dynamics in the dipole-octupole pyrochlore magnet  $\text{Ce}_2\text{Zr}_2\text{O}_7$ , *Phys. Rev. Lett.* **122**, 187201 (2019).
- [45] R. Sibille, N. Gauthier, E. Lhotel, V. Porée, V. Pomjakushin, R. A. Ewings, T. G. Perring, J. Ollivier, A. Wildes, C. Ritter, T. C. Hansen, D. A. Keen, G. J. Nilsen, L. Keller, S. Petit, and T. Fennell, A quantum liquid of magnetic octupoles on the pyrochlore lattice, *Nature Physics* **16**, 546 (2020).
- [46] V. Porée, H. Yan, F. Desrochers, S. Petit, E. Lhotel, M. Appel, J. Ollivier, Y. B. Kim, A. H. Nevidomskyy, and R. Sibille, Fractional matter coupled to the emergent gauge field in a quantum spin ice (2023), arXiv:2304.05452.
- [47] B. Gao, F. Desrochers, D. W. Tam, P. Steffens, A. Hiess, Y. Su, S.-W. Cheong, Y. B. Kim, and P. Dai, Emergent photons and fractionalized excitations in a quantum spin liquid (2024), arXiv:2404.04207 [cond-

- mat.str-el].
- [48] E. M. Smith, J. Dudemaine, B. Placke, R. Schäfer, D. R. Yahne, T. DeLazzer, A. Fitterman, J. Beare, J. Gaudet, C. R. C. Buhariwalla, A. Podlesnyak, G. Xu, J. P. Clancy, R. Movshovich, G. M. Luke, K. A. Ross, R. Moessner, O. Benton, A. D. Bianchi, and B. D. Gaulin, Quantum spin ice response to a magnetic field in the dipole-octupole pyrochlore  $\text{Ce}_2\text{Zr}_2\text{O}_7$ , *Phys. Rev. B* **108**, 054438 (2023).
- [49] D. R. Yahne, B. Placke, R. Schäfer, O. Benton, R. Moessner, M. Powell, J. W. Kolis, C. M. Pasco, A. F. May, M. D. Frontzek, E. M. Smith, B. D. Gaulin, S. Calder, and K. A. Ross, Dipolar spin ice regime proximate to an all-in-all-out néel ground state in the dipolar-octupolar pyrochlore  $\text{Ce}_2\text{Sn}_2\text{O}_7$ , *Phys. Rev. X* **14**, 011005 (2024).
- [50] S. H. Curnoe, Structural distortion and the spin liquid state in  $\text{Tb}_2\text{Ti}_2\text{O}_7$ , *Phys. Rev. B* **78**, 094418 (2008).
- [51] J. D. Thompson, P. A. McClarty, H. M. Rønnow, L. P. Regnault, A. Sørge, and M. J. P. Gingras, Rods of neutron scattering intensity in  $\text{Yb}_2\text{Ti}_2\text{O}_7$ : Compelling evidence for significant anisotropic exchange in a magnetic pyrochlore oxide, *Phys. Rev. Lett.* **106**, 187202 (2011).
- [52] K. A. Ross, L. Savary, B. D. Gaulin, and L. Balents, Quantum excitations in quantum spin ice, *Phys. Rev. X* **1**, 021002 (2011).
- [53] H. Yan, O. Benton, L. Jaubert, and N. Shannon, Theory of multiple-phase competition in pyrochlore magnets with anisotropic exchange with application to  $\text{Yb}_2\text{Ti}_2\text{O}_7$ ,  $\text{Er}_2\text{Ti}_2\text{O}_7$ , and  $\text{Er}_2\text{Sn}_2\text{O}_7$ , *Phys. Rev. B* **95**, 094422 (2017).
- [54] K. T. K. Chung, Mapping the Phase Diagram of a Frustrated Magnet: Degeneracies, Flat Bands, and Canting Cycles on the Pyrochlore Lattice (2024), to appear concurrently.
- [55] C. Xu, Gapless bosonic excitation without symmetry breaking: An algebraic spin liquid with soft gravitons, *Phys. Rev. B* **74**, 224433 (2006).
- [56] M. Pretko, Subdimensional particle structure of higher rank  $u(1)$  spin liquids, *Phys. Rev. B* **95**, 115139 (2017).
- [57] M. Pretko, Generalized electromagnetism of subdimensional particles: A spin liquid story, *Phys. Rev. B* **96**, 035119 (2017).
- [58] R. Moessner and J. T. Chalker, Properties of a classical spin liquid: The Heisenberg pyrochlore antiferromagnet, *Phys. Rev. Lett.* **80**, 2929 (1998).
- [59] R. Moessner and J. T. Chalker, Low-temperature properties of classical geometrically frustrated antiferromagnets, *Phys. Rev. B* **58**, 12049 (1998).
- [60] M. Taillefumier, O. Benton, H. Yan, L. D. C. Jaubert, and N. Shannon, Competing spin liquids and hidden spin-nematic order in spin ice with frustrated transverse exchange, *Phys. Rev. X* **7**, 041057 (2017).
- [61] O. Benton, L. Jaubert, H. Yan, and N. Shannon, A spin-liquid with pinch-line singularities on the pyrochlore lattice, *Nature Communications* **7**, 10.1038/ncomms11572 (2016).
- [62] D. Lozano-Gómez, V. Nocolak, J. Oitmaa, R. R. P. Singh, Y. Iqbal, J. Reuther, and M. J. P. Gingras, Competing gauge fields and entropically driven spin liquid to spin liquid transition in non-Kramers pyrochlores, *Proceedings of the National Academy of Sciences* **121**, e2403487121 (2024).
- [63] M. Pretko, X. Chen, and Y. You, Fracton phases of matter, *International Journal of Modern Physics A* **35**, 2030003 (2020).
- [64] R. M. Nandkishore and M. Hermele, Fractons, *Annual Review of Condensed Matter Physics* **10**, 295 (2019).
- [65] Y. You, Quantum liquids: Emergent higher-rank gauge theory and fractons (2024), arXiv:2403.17074 [cond-mat.str-el].
- [66] S. Vijay, J. Haah, and L. Fu, A new kind of topological quantum order: A dimensional hierarchy of quasiparticles built from stationary excitations, *Phys. Rev. B* **92**, 235136 (2015).
- [67] C. Chamon, Quantum glassiness in strongly correlated clean systems: An example of topological overprotection, *Phys. Rev. Lett.* **94**, 040402 (2005).
- [68] J. Haah, Local stabilizer codes in three dimensions without string logical operators, *Phys. Rev. A* **83**, 042330 (2011).
- [69] A. W. C. Wong, Z. Hao, and M. J. P. Gingras, Ground state phase diagram of generic  $xy$  pyrochlore magnets with quantum fluctuations, *Phys. Rev. B* **88**, 144402 (2013).
- [70] L. Savary, K. A. Ross, B. D. Gaulin, J. P. C. Ruff, and L. Balents, Order by quantum disorder in  $\text{Er}_2\text{Ti}_2\text{O}_7$ , *Phys. Rev. Lett.* **109**, 167201 (2012).
- [71] S. Guitteny, S. Petit, E. Lhotel, J. Robert, P. Bonville, A. Forget, and I. Mirebeau, Palmer-chalker correlations in the  $xy$  pyrochlore antiferromagnet  $\text{Er}_2\text{Sn}_2\text{O}_7$ , *Phys. Rev. B* **88**, 134408 (2013).
- [72] L. D. C. Jaubert, O. Benton, J. G. Rau, J. Oitmaa, R. R. P. Singh, N. Shannon, and M. J. P. Gingras, Are multiphase competition and order by disorder the keys to understanding  $\text{Yb}_2\text{Ti}_2\text{O}_7$ , *Phys. Rev. Lett.* **115**, 267208 (2015).
- [73] C. L. Sarkis, J. G. Rau, L. D. Sanjeeva, M. Powell, J. Kolis, J. Marbey, S. Hill, J. A. Rodriguez-Rivera, H. S. Nair, D. R. Yahne, S. Säubert, M. J. P. Gingras, and K. A. Ross, Unravelling competing microscopic interactions at a phase boundary: A single-crystal study of the metastable antiferromagnetic pyrochlore  $\text{Yb}_2\text{Ge}_2\text{O}_7$ , *Phys. Rev. B* **102**, 134418 (2020).
- [74] A. Bertin, Y. Chapuis, P. D. de Réotier, and A. Yaouanc, Crystal electric field in the  $\text{R}_2\text{Ti}_2\text{O}_7$  pyrochlore compounds, *Journal of Physics: Condensed Matter* **24**, 256003 (2012).
- [75] J. Gaudet, A. M. Hallas, A. I. Kolesnikov, and B. D. Gaulin, Effect of chemical pressure on the crystal electric field states of erbium pyrochlore magnets, *Physical Review B* **97**, 024415 (2017).
- [76] P. A. McClarty, S. H. Curnoe, and M. J. P. Gingras, Energetic selection of ordered states in a model of the  $\text{Er}_2\text{Ti}_2\text{O}_7$  frustrated pyrochlore  $xy$  antiferromagnet, *Journal of Physics: Conference Series* **145**, 012032 (2009).
- [77] J. G. Rau, S. Petit, and M. J. P. Gingras, Order by virtual crystal field fluctuations in pyrochlore  $xy$  antiferromagnets, *Phys. Rev. B* **93**, 184408 (2016).
- [78] S. Onoda and Y. Tanaka, Quantum fluctuations in the effective pseudospin- $\frac{1}{2}$  model for magnetic pyrochlore oxides, *Phys. Rev. B* **83**, 094411 (2011).
- [79] Y.-P. Huang, G. Chen, and M. Hermele, Quantum spin ices and topological phases from dipolar-octupolar doublets on the pyrochlore lattice, *Phys. Rev. Lett.* **112**, 167203 (2014).
- [80] N. Iwahara and L. F. Chibotaru, Exchange interaction



- between  $J$  multiplets, *Phys. Rev. B* **91**, 174438 (2015).
- [81] A. Sadeghi, M. Alaei, F. Shahbazi, and M. J. P. Gingras, Spin Hamiltonian, order out of a Coulomb phase, and pseudocriticality in the frustrated pyrochlore Heisenberg antiferromagnet  $\text{FeF}_3$ , *Phys. Rev. B* **91**, 140407 (2015).
- [82] N. Francini, L. Janssen, and D. Lozano-Gómez, Higher-rank spin liquids and spin nematics from competing orders in pyrochlore magnets (2023), [arXiv:2409.03825](https://arxiv.org/abs/2409.03825).
- [83] E. Belorizky, R. Casalegno, and J. J. Niez, Calculation of the spin wave energy gap at  $k = 0$  for a simple cubic ferromagnet with anisotropic exchange interactions, *Phys. Status Solidi B* **102**, 365 (1980).
- [84] M. E. Zhitomirsky and A. L. Chernyshev, *Colloquium* : Spontaneous magnon decays, *Rev. Mod. Phys.* **85**, 219 (2013).
- [85] A. Hickey, D. Lozano-Gómez, and M. J. P. Gingras, A Classical Chiral Spin-Liquid from Chiral Interactions on the Pyrochlore Lattice (2024), [arXiv:2403.02391](https://arxiv.org/abs/2403.02391) [[cond-mat.str-el](https://arxiv.org/abs/2403.02391)].
- [86] C. Castelnovo, R. Moessner, and S. L. Sondhi, Magnetic monopoles in spin ice, *Nature* **451**, 42 (2008).
- [87] M. Pretko, Subdimensional particle structure of higher rank  $U(1)$  spin liquids, *Phys. Rev. B* **95**, 115139 (2017).
- [88] M. Pretko, The fracton gauge principle, *Phys. Rev. B* **98**, 115134 (2018).
- [89] Y. Katayama, T. Mizutani, W. Utsumi, O. Shimomura, M. Yamakata, and K. Funakoshi, A first-order liquid-liquid phase transition in phosphorus, *Nature (London)* **403**, 170 (2000).
- [90] L. Henry, M. Mezouar, G. Garbarino, D. Sifré, G. Weck, and F. Datchi, Liquid-liquid transition and critical point in sulfur, *Nature (London)* **584**, 382 (2020).
- [91] M. Beye, F. Sorgenfrei, W. F. Schlotter, W. Wurth, and A. Fohlich, The liquid-liquid phase transition in silicon revealed by snapshots of valence electrons, *Proc. Natl. Acad. Sci. U.S.A.* **107**, 16772 (2010).
- [92] J. N. Reimers, Absence of long-range order in a three-dimensional geometrically frustrated antiferromagnet, *Physical Review B* **45**, 7287 (1992).
- [93] J. Villain, Insulating spin glasses, *Zeitschrift für Physik B - Condensed Matter* **33**, 31 (1979).
- [94] H. Kadowaki, H. Takatsu, T. Taniguchi, B. Fåk, and J. Ollivier, Composite spin and quadrupole wave in the ordered phase of  $\text{Tb}_{2+x}\text{Ti}_{2-x}\text{O}_{7+y}$ , *SPIN* **05**, 1540003 (2015).
- [95] C. Castelnovo and R. Moessner, Rod motifs in neutron scattering in spin ice, *Phys. Rev. B* **99**, 121102 (2019).
- [96] J. D. Alzate-Cardona, D. Sabogal-Suárez, R. F. L. Evans, and E. Restrepo-Parra, Optimal phase space sampling for Monte Carlo simulations of Heisenberg spin systems, *J. Phys. Condens. Matter* **31**, 095802 (2019).
- [97] M. E. Zhitomirsky, M. V. Gvozdkova, P. C. W. Holdsworth, and R. Moessner, Quantum Order by Disorder and Accidental Soft Mode in  $\text{Er}_2\text{Ti}_2\text{O}_7$ , *Phys. Rev. Lett.* **109**, 077204 (2012).
- [98] M. Creutz, Overrelaxation and Monte Carlo simulation, *Phys. Rev. D* **36**, 515 (1987).
- [99] J. G. Rau and M. J. P. Gingras, Spin slush in an extended spin ice model, *Nat. Comm.* **7**, 12234 (2016).
- [100] K. T. K. Chung and M. J. P. Gingras, 2-form  $u(1)$  spin liquids: Classical model and quantum aspects (2023), [arXiv:2310.17607](https://arxiv.org/abs/2310.17607) [[cond-mat.str-el](https://arxiv.org/abs/2310.17607)].
- [101] H. Yan, O. Benton, L. D. C. Jaubert, and N. Shannon, Rank-2  $u(1)$  spin liquid on the breathing pyrochlore lattice, *Phys. Rev. Lett.* **124**, 127203 (2020).
- [102] V. Noculak, D. Lozano-Gómez, J. Oitmaa, R. R. P. Singh, Y. Iqbal, M. J. P. Gingras, and J. Reuther, Classical and quantum phases of the pyrochlore  $s = \frac{1}{2}$  magnet with Heisenberg and Dzyaloshinskii-Moriya interactions, *Phys. Rev. B* **107**, 214414 (2023).
- [103] K. T. K. Chung, J. S. K. Goh, A. Mukherjee, W. Jin, D. Lozano-Gómez, and M. J. P. Gingras, Probing flat band physics in spin ice systems via polarized neutron scattering, *Phys. Rev. Lett.* **128**, 107201 (2022).
- [104] P. H. Conlon and J. T. Chalker, Absent pinch points and emergent clusters: Further neighbor interactions in the pyrochlore Heisenberg antiferromagnet, *Phys. Rev. B* **81**, 224413 (2010).
- [105] D. A. Garanin and B. Canals, Classical spin liquid: Exact solution for the infinite-component antiferromagnetic model on the kagomé lattice, *Phys. Rev. B* **59**, 443 (1999).
- [106] B. Canals and D. A. Garanin, Classical spin liquid properties of the infinite-component spin vector model on a fully frustrated two dimensional lattice, *The European Physical Journal B - Condensed Matter and Complex Systems* **26**, 439 (2002).
- [107] B. Canals and D. A. Garanin, Spin-liquid phase in the pyrochlore anti-ferromagnet, *Canadian Journal of Physics* **79**, 1323 (2001), <https://doi.org/10.1139/p01-101>.